Supporting Online Material for

Structure and Formation of the Lunar Farside Highlands

Ian Garrick-Bethell,* Francis Nimmo, Mark A. Wieczorek

*To whom correspondence should be addressed. E-mail: igarrick@ucsc.edu

Published 12 November 2010, *Science* **330**, 949 (2010)
DOI: 10.1126/science.1193424

This PDF file includes:

Structure and Formation of the Lunar Farside Highlands

Ian Garrick-Bethell*[1†], Francis Nimmo[2], and Mark A. Wieczorek[3]

[1]Department of Geological Sciences, Brown University
[2]Department of Earth and Planetary Sciences, University of California, Santa Cruz
[3]Institut de Physique du Globe de Paris
*To whom correspondence should be addressed: igarrick@ucsc.edu
†Now at: Department of Earth and Planetary Sciences, University of California, Santa Cruz

Supporting Online Material

List of sections

1. Details on the degree-2 shape of the lunar farside

1.1 *Data, calculation of average topography, and calculation of best fit function*

The topography swaths plotted in Fig. 1a were obtained using the March 16, 2010 version of Lunar Reconnaissance Orbiter (LRO) Lunar Orbiter Laser Altimeter (LOLA) 4 pixel-per-degree gridded data, downloaded from the Planetary Data Service. The data are referenced to a sphere of radius 1737.4 km. No correction for the present day hydrostatic dynamical flattening was made, since this effect is of the order 10 m (e.g. (*S1*)), and no center-of-mass/center-of-figure offset corrections were applied. The data were downsampled to 1-pixel-per-degree in order to remove short wavelength topography. This downsampling provides more than adequate resolution to observe degree-2 topography trends over ~100° of great circle arc. In addition, this resolution more closely matches the low resolution of the crustal thickness model that we use in our analysis. The background map in all topography figures is 4 pixel-per-degree LOLA data.

The crustal thickness model was calculated using the methodology outlined in (*S2, 3*), and made use of LOLA topography data combined with Kaguya gravity model SGM100h (*S4*). The density of both the crust and mantle were assumed to be independent of depth and position, and

the mare basalts were accounted for in the major mascon basins as in the previous models of (*S2*, *3*) (the basalt flows within the limits of the Degree Two Terrane (DTT) are not subtracted, see Section 2). This model assumes a crustal density of 2800 kg m^{-3}, a mantle density of 3360 kg m^{-3}, and a density of 3100 kg m^{-3} for the mare basalts. The maximum spherical harmonic degree used in our invervion for the crust-mantle interface was 70 (the gravity model SGM100h used an a priori constraint at degrees higher than this), and the filter applied to the Bouguer anomaly was set to 0.5 at degree 50, which is significantly less restrictive than used in the pre-Kaguya models. The final map product used for our calculations has a resolution of 1 pixel-per-degree.

When inverting for the relief along the crust mantle interface, it is necessary to either assume an average crustal thickness, or to anchor the inversion to a known value at a specific location. Here, we choose the average thickness of the crust to be 46.6 km, which yields a crustal thickness of zero beneath the Moscoviense basin (see also (*S5*)). The model's crustal thickness between the Apollo 12 and 14 sites is 37.8 km, which is consistent with the seismic constraint of 38 ± 8 from (*S6*), but a little larger than the value of 30 ± 2.5 from (*S7*). High frequency oscillations that are present on the farside between the equator and 60° N and between 30° W and 30° E are due to the limited Kaguya tracking data in this region (not readily visible in the crustal thickness swaths).

All map projections are Mollweide, except in Fig. S4 and S6, which use simple cylindrical grids.

The swaths in Fig. 1 and all other similar figures were calculated from transects obtained in two opposite directions. The "fit direction" is used to fit the topography data, and is black in Fig. 1a and 1c. An extra amount of data in this direction is included in blue to show the topography trend beyond the region fitted. The "prediction" direction is used to test if the topography fit accurately predicts the topography in the opposite direction, and is shown in blue. All of the swaths in this paper were calculated by averaging data between two great circle transects emanating from a common latitude and longitude. For the fit direction, the azimuth of the first great circle transect is defined by the angle φ, as shown in Fig. S1. The azimuth of the second great circle transect is defined by the angle $\varphi + \theta$, where θ is the swath width. The mean topography in the swath between φ and $\varphi + \theta$ was calculated by averaging great circle transects between the angles φ and $\varphi + \theta$ (Fig. S1), with each transect having an angular separation of 1 degree. The prediction swaths are obtained in the same way for data between $\varphi + 180°$ and $\varphi + \theta + 180°$. The angle ψ represents the length of the great circle arc. The bilinear interpolation scheme used in calculating the great circle transects used the same number of interpolated points as the number of degrees in the transect, thereby accurately representing the resolution of the LOLA and crustal thickness 1-pixel-per-degree data.

Nonlinear least squares regressions to a degree-2 Legendre polynomial, P_2, were performed for the mean topography profiles $y(x)$, where x is an angular distance:

$$y(x) = \alpha P_2 + \beta \qquad (1)$$

where P_2 is

$$P_2 = \frac{1}{2}(3\cos^2(x) - 1) \quad (2)$$

Fitting the data in this manner makes α analogous to an expansion coefficient in the spherical harmonic representation of topography, where the spherical harmonics are Legendre polynomials. Note that these equations assume that the topography data start at the highest or lowest elevation of the degree-2 harmonic, *i.e*. they allow for no phase dependence. This is acceptable in this application because we started our analysis by searching for the peak of the degee-2 topography, and used the peak as an origin. The term β appears because the local topography or crustal thickness may have an arbitrary offset to the global mean radius. The fits in Fig 1a and 1c and other similar figures were typically performed over great circle arcs of ψ = 90-110°. The 95% confidence intervals for the fit topography were also calculated and shown beyond the fit area as dashed blue lines around the fit line. Table S1 gives a summary of all topography fits presented in the paper.

Table S1. Summary of swath dimensions and least squares fits to P_2 for LOLA topography

Swath	Fig.	Lat. °N*	Lon. °E*	φ°	θ°	Ψ°	α (km)†	β (km)†	R^2
1	1	23	198	0	90	100	4.08 ± 0.17	4.15 ± 0.17	0.98
2	1	-10	217	80	10	105	4.70 ± 0.21	5.65 ± 0.21	0.98
3	1	0	217	-45	10	100	3.65 ± 0.43	5.40 ± 0.42	0.93
4	1	7	210	40	10	95	4.79 ± 0.24	4.83 ± 0.22	0.98
5	1	-9	223	0	90	100	4.00 ± 0.29	4.39 ± 0.29	0.96
6	S2	-10	217	90	10	105	4.25 ± 0.33	4.85 ± 0.34	0.94
7	S2	0	217	0	10	100	4.01 ± 0.16	5.31 ± 0.15	0.99
8	S2	9	211	-30	10	95	4.83 ± 0.36	5.62 ± 0.34	0.96
9	S4/S5	-84	194	0	90	105	-4.80 ± 0.18	-3.92 ±0.18	0.98
10	S4/S5	78	74	0	90	105	-3.02 ± 0.15	-1.13 ± 0.15	0.99
11	S7	-90	0	-90	45	180	-0.1 ± 0.26	-0.80 ± 0.24	<0.01
12	S7	-90	0	-45	45	180	-0.44 ± 0.18	-1.62 ± 0.17	0.12
13	S7	-90	0	0	45	180	-0.42 ± 0.28	-1.14 ± 0.26	0.05
14	S7	-90	0	45	45	180	-0.49 ± 0.16	-1.53 ± 0.15	0.17
15	S7	-90	0	225	45	180	2.75 ± 0.19	2.63 ± 0.18	0.82

* Latitude and longitude indicates the origin point for all swaths Note that for swaths 11-15, the origin latitude and longitude is at the south pole, and the swath extends upwards to the north pole (see Fig S6).
† 95% confidence intervals are shown for the coefficients α and β.

1.2 *Additional swaths that show degree-2 structure*

Three additional swaths (#6-8) similar to those in Fig. 1 are presented in Fig. S2 for both topography and crustal thickness, in order to demonstrate the robustness and scale of the degree-2 structure. A comparison between these swaths and calculated crustal thickness from tidal dissipation, for the tidal model discussed in the main text (T_b = 1175 °C), is shown in Fig. S3, similar to Fig. 2. Note the match in swath 6 from -90 to +55°, which may represent a degree-4 harmonic that appears in our tidal dissipation calculations (main text and Section 5.5, Fig. S10).

1.3 *Uniqueness of degree-2 topography on the lunar farside*

Sums of spherical harmonics can be used to describe arbitrary distributions of topography and gravity data on a sphere. However, the existence of an isolated geophysical feature that is

described almost entirely by a single harmonic wavelength, other than rotational flattening, is uncommon. To demonstrate the uniqueness of the degree-2 fits in the farside highlands, we performed the swath fitting routine described above to the entire Moon. Specifically, we calculated topography swaths with φ = 0°, θ = 90°, and ψ = 105° (similar to swaths 1 and 5), while allowing for either positive or negative α, and calculated the correlation coefficient R^2 at all points on a lunar sphere with 2° grid spacing in latitude in longitude. A simple cylindrical projection of the resulting R^2 values is shown in Fig. S4a-c. Fig. S4a plots the values of R^2 without any contrast enhancement, and it is clear that the farside highlands emerge as an island of high R^2.

Figure S4b and Fig. S4c show the R^2 grid contrasted to highlight only regions with $R^2 > 0.8$, and $R^2 > 0.95$, respectively. Two regions outside of the farside highlands emerge as having high quality fits ($R^2 > 0.8$), as indicated by the two arrows in Fig. S4b. However, their high quality fits are actually due to their proximity to the farside highlands. Representative topography and fits for the two high R^2 regions are shown as topography swaths 9 and 10 in Fig. S5. Both swaths start at low topography and end at high topography. When the swaths are plotted on the lunar globe, as in Fig. S5b, it becomes clear that the swaths start outside the farside highlands and their azimuths point them directly at the farside highlands. Swath 9 crosses portions of the South-Pole-Aitken basin, and some of its upward topography trend may be a superposition of the basin topography on preexisting background degree-2 farside topography. In addition swaths 9 and 10 do not have the same agreement between the predicted and actual topography for data between azimuths φ = 180° and 270° (leftmost blue portions of Fig. S5a), as for swaths 1-3 in the farside highlands (Fig. 1a). Note that the leftmost portion of swath 9 contains mare Australe, and therefore it is not clear to what extent this terrain may have been modified since the formation of any degree-2 structure there. In sum, these two regions of high R^2 are not representative of a separate degree-2 trend elsewhere on the Moon, and they are not indicative of a general phenomenon of high quality degree-2 fits at arbitrary locations on the Moon.

1.4 *Center of the Degree Two Terrain*

Figure S4 is also helpful in assessing the approximate center of the DTT. From Fig. S4c, the center of the farside highlands with high R^2 is at approximately (5° N, 210° E). We may also perform the same analysis as above except with φ = -90° and θ = 180°, in order to capture more of the terrain. The result is shown in Fig. S6, where an island of high R^2 again appears in the farside highlands (an arcuate section of terrain to the east of the farside highlands has high R^2 because it is the eastern topographic low of the DTT). The approximate center of the terrain in Fig. S6 is near (10° N, 210° E). However, taking into account the approximate centers of the regions of thickest crust and highest topography, a center of (0° ± 5° N, 215° ± 5° E) is a more reasonable best estimate. Knowledge of the exact center is difficult to assess given the long wavelength of the feature, its asymmetric preservation, and the presence of several 100-km-scale basins near the DTT center. However, it is not critical to know the exact center in order to determine the extent of the DTT, or test the hypothesis that the DTT is related to tidal processes.

1.5 *Relationship with the Moon's degree-2 gravity and topography spherical harmonic coefficients*

It has been known for some time that the Moon possesses relatively high degree-2 power in its gravity and topography spherical harmonic expansions, e.g. (*S8-10*). However, the degree-2 terms of global expansions of topography and gravity and the detailed distributions of these datasets on the Moon are different problems, and we are justified in seeking regional variations in long-wavelength topography. For example, given that the Moon has a high degree 2 and order 0 spherical harmonic gravity coefficient C_{20}, we might naively assume that there is a strong increase in degree-2 topography when moving from the pole to the equator at all locations on the Moon. However, in Fig. S7 we plot four swaths (#11-14) of nearside topography from pole to pole that show no appreciable long wavelength topography. The four swaths have widths of 45° and together they capture all of the nearside data (detailed parameters in Table S1). Fits to P_2 were performed with the constraint that the maximum or minimum amplitude of the oscillation occurs at the equator, which is justified in the case of looking for examples of the C_{20} and C_{22} (degree 2 and order 2) power of the Moon. No equator-centered degree-2 trend is obvious from the plots. The quality of the fits are poor ($R^2 < 0.17$), although other intermediate wavelength trends such as the relatively low elevation of mare units in the north, are apparent. An additional swath (#15) and high quality P_2 fit on the farside between longitudes 225° and 270° is shown for comparison ($R^2 = 0.82$). Therefore, as discussed by (*S10*), a complete understanding of the long-wavelength topography of the Moon must be done by considering the detailed effects of geology, rather than global low degree metrics alone.

1.6 *Polynomial fits to the farside degree-2 shape*

In the main text we argue that a reasonable explanation for the degree-2 topography of the farside is tidally-driven crustal thickness differences. To strengthen this argument, we show that arbitrary polynomial fits, where the argument of the polynomial is x, and *not* cos(x), are poorer fits to the topography than a degree-2 harmonic. Because the degree-2 topography trend is broken in some places by the South Pole-Aitken basin and other regional geologic features (see main text), we perform our fitting on three swaths that contain relatively unbroken trends in topography, swaths 1-3 in Fig. 1a. In Fig. S8a-c we fit progressively higher order polynomials, $Q_n(x)$, to topography in swaths 1 and 2 (plotted in black). The value of R^2 for the 3rd and 4th order polynomials are comparable to those of a degree-2 harmonic for both swaths 1 and 2, but the predicted topography (leftmost blue portions of Fig. S7) is a much poorer fit with the polynomials. Fitting higher order polynomials is not warranted based on the already-high value of R^2 for degrees 3 and 4, and would be an exercise in over-fitting. Similar results are found for crustal thickness (Fig. S8d-e). Therefore, with the observation that the major topography and crustal thickness change in the farside highlands takes place over ~90° of arc, and the excellent fits and predictive power of a P_2 function compared with other functions, we conclude with high confidence that the gross structure of the lunar farside highlands is described by a degree-2 oscillation.

Note that degree-3 and degree-4 Legendre polynomials (with cos(x) arguments) contain higher frequency oscillations (inflections at < 90° of arc) than the structure of the DTT, and will be much poorer fits to the topography and crustal thickness.

1.7 *P_1 or cos(x) function fit to the farside degree-2 shape*

We also fit farside crustal thickness data to a P_1 or cos(x) function. We performed the fit for a swath of terrain very similar to swath 1, except that φ = -10° (instead of φ = 0°), and the fit included the prediction terrain for 100° of arc, for a fit over a total of 200° of arc. We also performed the fit to the usual fit region of swath 5 (100° of arc). These swaths are used here because they average over a wide range of topography and average out the effects of small craters. In Fig. S9a and S9b we compare the cos(x) fits to the P_2 fits for the slightly modified swath 1 and unmodified swath 5, respectively, and in Fig. S9c and S9d we show the residuals of these fits, respectively.

In examining Fig. S9a and S9b, it is clear both from the fits and R^2 values that the P_2 function is a better fit for both swaths. The residuals in Fig. S9c and S9d reinforce this conclusion. Ideally, residuals are evenly distributed, in which case they represent random errors about the best-fit function. The residuals for the P_2 function are approximately evenly distributed, and appear to have no obvious structure, suggesting a P_2 function is a good choice. However, the residuals for the cos(x) fit are symmetric about zero, and have a clear periodicity. The residuals for cos(x) also change sign near -90° and 90°, where the minima of the P_2 function are located. While only 100° of fit is shown in Fig. S9b and S9d for swath 5, the same residuals structure as in Fig. S9c is observed. Note that the degrees of freedom are the same in the cos(x) and P_2 fits, such that the higher quality fit for P_2 is not the result of additional free parameters. Therefore, we conclude that the P_2 function is unequivocally a better fit than a cos(x) function.

Note that the results for the original swath 1 (φ = 0°), fit over 200° of arc are the same (R^2 for cos(x) = 0.82, R^2 for P_2 = 0.92, not shown), except that the overall fit is slightly lower quality in both cases.

2. Mare thickness effect on topography and crustal thickness profiles

The swaths of topography and crustal thickness in Fig. 1 and S2 cross into Oceanus Procellarum and Mare Frigoris. Mare basalt flows in these regions are rarely > 1 km (*S11-14*), while the amplitude of the DTT topography is ~6.4 km (mean of fits to swaths 1-5), and the crustal thickness amplitude is ~36 km (main text). Therefore, it is not surprising that the mare thicknesses are not immediately visible in the swath profiles. A more detailed study of crustal thicknesses across the border of Oceanus Procellarum and Mare Frigoris, would be worthwhile, however.

3. Gravity anomaly expected from uncompensated and compensated degree-2 terrain

Uncompensated global degree-2 topography of 6 km amplitude would have an anomaly of ~300 mgal (*S8*), and compensated terrain would have an anomaly of ~15 mgal. Because the gravity anomalies over the lunar farside are much lower than 300 mgal (*S4*), the terrain there must be largely compensated (*S15*).

4. Orbit evolution calculations

To estimate the Moon's distance from the Earth as a function of time, we use equation 4.214 of (*S16*). We assume the Earth's tidal potential Love number is 0.3, similar to present values (*S17*), and a tidal specific dissipation factor between 100-250. The range of tidal specific dissipation factors is used because the conditions on the early Earth may have been much different than they are presently. For example, the present dissipation factor of ~12 is due largely to dissipation in the oceans, while the present value for the solid Earth alone is ~280 (*S18*), and it is not clear where in between these two values the very early Earth would reside. It is easy to establish that dissipation in the Earth is higher than in the past based on integrations of its orbital evolution (e.g. (*S17*)). See also Section 5.3.

5. Tidal heating in a floating crust

5.1 *Introduction*

Tidal dissipation in the Moon has been previously considered for the case of a completely solid sphere (*S19*), in which case its contribution to lunar thermal evolution is negligible. However, in satellites with a crust decoupled from the mantle by a subsurface ocean, tidal dissipation in the crust is enhanced and can lead to global crustal thickness variations due to differences in the spatial distribution of tidal heating (*S20-23*). The previous studies on this dissipative process have dealt with oceans composed of liquid water and crusts of ice in thermal equilibrium with tidal heating. In the case of the Moon, the solid crust is largely anorthosite, and the liquid is the remaining liquids from the magma ocean. The Moon's rocky crust has a much stronger resistance to tidal deformation than ice, but it also has a much higher basal temperature that controls the crust's viscosity and tidal dissipation. It can be shown that non-negligible crustal thickness differences can be established for reasonable orbital properties and magma ocean temperatures, assuming the crust is in equilibrium with tidal heating. These crustal thickness differences have a strong degree-2 component that can plausibly explain the degree-2 structure of the DTT.

5.2 *Coupled tidal heating and crustal thickness model*

To model the tidal dissipation in the lunar crust overlying a liquid magma ocean, we adopt a tidal heating model originally developed by (*S21*). Our implementation is described in some detail in (*S20*) and thus only a brief overview is given here.

A synchronous satellite with non-zero eccentricity experiences a time-varying tidal potential, which may in turn result in tidal heating (*S19*). In a shell which is thin compared to the satellite's radius, each component of the diurnal tidal strain rate tensor $\dot{\varepsilon}_{ij}$ varies with position but not depth, and has a magnitude given by

$$\dot{\varepsilon}_{ij} = f\left(\frac{h_{2t}}{2.5}\right)\frac{\tilde{n}^3 R_s^3}{GM_s}e \qquad (3)$$

where h_{2t} is the tidal potential Love number, $\tilde{n}$ is the mean motion, R_s and M_s are the satellite radius and mass, respectively, G is the gravitational constant, e is the orbital eccentricity and f is a longitude and latitude dependent function of order unity (*S21*). We assume zero obliquity for simplicity. We calculate $\tilde{n}$ from $(GM_p/a^3)^{1/2}$, where M_p is the primary (Earth) mass and a the semi-major axis. Higher eccentricities, faster periods, and more deformable bodies lead to larger diurnal tidal strain rates; strain rates in thin shells are higher at the poles and lower at the equator. When the shell is decoupled from the mantle by a liquid layer, the net dissipation per unit volume increases in the shell because h_{2t} increases.

Assuming that the shell can be described as a Maxwell viscoelastic material, the local heating rate W is given by

$$W(\omega, \lambda, \eta) = \frac{2\mu \bar{\varepsilon}_{ij}^2}{\tilde{n}} \left[\frac{n\tau_M}{1 + (n\tau_M)^2} \right] \quad (4)$$

Here ω and λ are the longitude and latitude, η is the local viscosity, μ is the rigidity, $\tau_M = \eta / \mu$ is the Maxwell time and an overbar denotes time-averaging over one tidal cycle. Dissipation is large when the Maxwell time is comparable to the tidal (forcing) period.

The viscosity of the crust is a critical parameter that controls the dissipation rate. To model the viscosity, we assume that the lunar crust is predominantly composed of anorthite. Experimental measurements show that the viscosity of anorthite is temperature-dependent and non-Newtonian but not grain-size dependent (*S24*). We use a flow low for dry anorthite (0.004 weight % H_2O) (*S24*). We must account for the temperature (and thus depth) and stress dependence of the crust's viscosity to accurately model tidal dissipation. The viscosity at the base of the crust $\eta_b(T_b)$ is calculated as follows:

$$\eta_b(T_b) = \frac{1}{V} \sigma_t^{1-n} \exp\left(\frac{Q}{RT_b}\right) \quad (5)$$

Here T_b is the temperature at the base of the crust, V is a material constant, Q is the activation energy and σ_t is the characteristic tidal stress, taken to be $\mu\bar{\dot{\varepsilon}}/n$, where $\bar{\dot{\varepsilon}}$ is the local, time-averaged strain rate. Because the temperature is highest at the base of the crust, the viscosity and tidal dissipation there is generally highest.

To calculate the variation of viscosity with temperature, and thereby depth, we use a linearized version of equation (5), termed the Frank-Kamenetskii approximation, which gives

$$\eta(T) = \eta_b \exp[-\gamma(T - T_b)] \quad (6)$$

where T is temperature, and γ is a constant which depends on the activation energy of the shell material.

In the classic problem of tidally-produced shell thickness variations on Europa (*S21*), the floating crust is in conductive thermal equilibrium with internal tidal heating and the basal heat flux into the crust. That is, the crust is thick enough such that the steady state internal heating

and temperature distribution yields melting temperatures at the crust's base. In the case of the Moon, however, the subsurface magma ocean liquid is cooling, resulting in loss of latent heat and growth of the crust, and therefore the crust is not in steady state equilibrium. If the cooling is slow, and governed by the loss of latent heat through conduction up the crust, as in the case of the classic Stefan problem (*S25*), one may assume that the crustal thickness is in quasi-equilibrium with the effective basal heat flux due to magma ocean cooling alone. Specifically, if the rate of cooling is slower or comparable to the rate of change of tidal heating, then one may assume that the crust is also in quasi-equilibrium with tidal heating. This is often the case since tidal heating is a very strong function of semimajor axis and time, and the crust cools at a mean rate of ~1 mm per year (assuming ~50 my cooling times). This approximation would be sufficient for small amplitude crustal thickness variations, but becomes less accurate for large amplitudes. Therefore, in this paper we restrict our analysis to the Europa-like scenario, where the crust has reached true conductive thermal equilibrium with the background heat flux from radiogenic heat from magma ocean liquids, and cooling of the underlying hot mantle cumulates, such that the crust can no longer grow by cooling and crystallizing the magma ocean. This is the assumption for the two cases reported in the main text for T_b = 1175 °C and T_b = 1225 °C, (q_o = 27 mW/m^2 and q_o = 30 mW/m^2), and assumes that some liquid remains at this time. The approximate value of q_o is derived in Section 10. In the future, additional studies can be done for tidal dissipation while the crust is still growing.

In order to determine the equilibrium crustal thickness in the shell due to internal tidal dissipation W and basal heat flux q_o, we must solve the steady-state heat conduction equation

$$\nabla^2 T + \frac{W(z)}{k} = 0 \qquad (7)$$

where k is the thermal conductivity (assumed constant). We solve this equation to determine the equilibrium shell thickness D at a point subject to the boundary conditions of a specified, spatially-varying surface temperature, a specified q_o, and a specified T_b. Because the heat production W depends on the temperature via the viscosity, we use a finite-difference shooting technique to estimate the steady state temperature and crustal thickness distribution (*S20*). The temperature gradient at the base of the crust is set by the basal heat flux. We numerically integrate equation (7) upwards to calculate the surface temperature. We then update the crustal thickness depending on the difference between the calculated and required surface temperature, and iterate until the required surface temperature is obtained.

The mean diurnal near-surface temperature influences the temperature gradient from the surface to the liquid layer, and thereby affects the equilibrium crustal thickness. We calculate the mean near-surface temperature using the same method as (*S21*), assuming that the inclination is 2^o and the product (1-A_b)F_s is 750 Wm^{-2}, where A_b is the albedo and F_s the insolation. This results in mean equatorial and polar temperatures of 254 and 101 K, respectively, close to the values calculated by (*S26*).

We nominally assume no internal heat generation in the crust due to radioactive decay. Nominal parameters adopted are given in Table S2.

Table S2. Nominal parameters in tidal heating and crustal thickness model

Parameter	Value	Units
κ	6×10^{-7}	$m^2\ s^{-1}$
h_{2t}	1.25	-
N	3	-
γ	$Q/R_qT_b^2$	K^{-1}
M_s	7.35×10^{22}	kg
ρ_c	2900	$kg\ m^{-3}$
k	1.8	$W\ m^{-1}\ K^{-1}$
Q	648*	$kJ\ mol^{-1}$
R_g	8.34	$J\ K^{-1}\ mol^{-1}$
R_s	1737	km
$\Delta\rho_{cl}$	100	$kg\ m^{-3}$
μ	100	GPa
$\mathrm{Log}_{10}(V)$	12.7*	$MPa^{-n}\ s^{-1}$
M_p	6×10^{24}	kg

*Values for dry (0.004wt% water) anorthite from (*S24*).

5.3 *Orbital parameters and basal temperatures*

There are several constraints on the plausible range of the critical parameters *a*, *e*, and T_b for which we may explore tidal dissipation and crustal thickness variations. We will consider them each separately.

The value of *a* increases with time after accretion, as does the crustal thickness due to cooling. Generally, at very early times the Moon will have a thin crust and high dissipation due to its close proximity to the Earth, and at later times it will have a thicker crust, and weaker dissipation due to its distance from the Earth. The Moon's crust formed in 20-100 My (*S27, 28*), and likely retained a liquid surface for < 10^5 years due to rapid heat loss by radiative cooling (*S29*). Using the tidal parameters in Section 4, it takes roughly ~0.1-0.3 My to evolve to $a = 10R_E$ (R_E = 1 Earth radius), ~2-4 My to $a = 15R_E$, and ~10-25 My to $a = 20R_E$. Based on the cooling timescale calculations of (*S27*), at these distances and times, crustal thicknesses are of the order of ~0-1 km, 1-10 km, and tens of km, respectively. It is important to note that as the crust thickens, the total internal dissipation increases, such that greater values of mean crustal thickness at later times may result in large absolute crustal thickness differences, offsetting the reduced dissipation at greater distances from the Earth.

The value of *e* during crust formation is uncertain. The present lunar eccentricity of 0.055 is increasing at a rate of ~0.014 by^{-1} (*S30*), and it has likely been increasing for a significant portion of lunar history due to dissipation in the Earth (*S30-32*). Crude backwards extrapolation of the present eccentricity rate would yield an eccentricity of -0.006 4.5 by ago. The dissipation in the Earth must have been lower in the past (*S32*) (as evidenced by a simple tidal evolution model that would place the Moon in its present location in < 2 By using present tidal parameters), such that the past eccentricity rate was likely lower. The early eccentricity may have been excited by resonances described in (*S33*), or have some component left over from accretion processes (*S34*) (~0.01). Other planetary resonances may have affected the eccentricity beyond $25R_E$ (*S35*). We explore values of e = 0.015 to 0.02 for a = 15 to $20R_E$. Note that tidal dissipation increases like

e^2. Note also that uncertainty in e is offset by uncertainty in a number of other parameters (e.g. Section 5.7).

The value T_b has a critical effect on the viscosity profile of the entire crust. The high activation energy of dry anorthite means that small differences in temperature will result in large differences in viscosity and dissipation. The value of T_b should be approximately equal to the temperature of the magma ocean. As the magma ocean crystallizes, its temperature is reduced, and viscosity and dissipation decrease, adding to the reduction in dissipation due to growth of a alone. A discussion of expected temperatures in the magma ocean is given in Section 9.

5.4 *Crustal thickness dependence on choice of parameters*

In the main text we reported crustal thickness results for $a = 20R_E$, $e = 0.02$, $T_b = 1175$ °C, and $q_o = 27$ mW/m^2, yielding a maximum crustal thickness of 71 km, a minimum of 50 km, and a mean of 65 km, for a net difference of 21 km. However, the observed crustal thickness difference is ~36 km, which may reflect uncertainty in our choice of parameters. Therefore, to compare the *shape* of the modeled and observed datasets in the main text, we multiplied the observed crustal thickness by 0.4. Higher dissipation as a result of higher basal temperatures, different rheological parameters, or dissipation in a partially molten region (Section 5.7) would produce higher dissipation and net crustal thickness differences comparable to the observed values. For example, the other case given in the main text is $a = 20R_E$, $e = 0.02$, and $T_b = 1225$ °C, $q_o = 30$ mW/m^2. This yields a minimum of 24 km, a maximum of 68 km, and a mean of 39 km, with a net difference of 44 km, close to the observed values. In Fig. S10 we show this case and compare it to the observed crustal thickness without any scaling factor. The agreement of the shapes is even better than the cases shown in Fig. 2, in part because the higher dissipation more strongly overcomes the surface temperature effect. In this case there is also agreement in amplitude, and it therefore represents strong evidence that the shape of the lunar farside crust can be described by a tidal dissipation process, albeit with numerous parameters that are difficult to constrain precisely.

In Table S3 we list a number of other cases that show the dependence of the crustal thickness distribution on orbital and thermal parameters.

If tidal dissipation is insignificant, a crustal thickness difference will result entirely from the pole-to-equator surface temperature (insolation) effect. For example, a case that does not produce any significant crustal thickness differences due to tidal heating is: $a = 25R_E$, $e = .015$ and $T_b = 1175$ °C, producing a maximum and minimum crustal thickness of 47.1 km (equator) and 42.9 km (pole), respectively, for a net difference of 4 km, and a mean of 43.5 km, for a basal heat flux of 50 mW/m^2, and a resulting surface heat flux of 50.04 mW/m^2 (the basal heat flux in this example is not an important parameter).

If we include the effects of additional heating from upper crustal radioactivity, the mean crustal thicknesses decreases, while the net crustal thickness difference stays approximately the same as without the additional heating. Case 4 in Table S3 includes internal heating as defined by equation 18 in Section 10, and the associated parameters 4.4 by ago, while Case 3 in Table S3 uses the same tidal and thermal parameters with no internal radiogenic heating. The maximum

and minimum crustal thicknesses are different by 5 km, the mean thicknesses are different by 3 km, and the amplitudes are the same. For simplicity, we have not included this effect in the model calculations.

Table S3. Tidal heating models and crustal thickness differences

Case	Fig.	a (R_E)	e	T_b °C	Net diff. km	Max. km	Min. km	Mean km	Basal heat flux mW/m^2	Surface heat flux mW/m^2
1	2, S3,S11	20	0.02	1175	21	78	57	68	27	31.2
2	S10	20	0.02	1225	44	68	24	39	30	56.1
3	-	20	0.02	1175	16	71	55	63	30	33.7
4*		20	0.02	1175	16	66	50	60	30	42.2
5	-	20	0.02	1175	5	53	48	51	40	42.6
6	-	20	0.02	1150	7	78	71	75	27	28.4
7	-	22	0.02	1175	5	79	74	77	27	28.2
8	-	22	0.025	1175	17	79	62	73	27	30.2
9	-	18	0.015	1175	23	78	55	70	27	31.7
10	-	20	0.015	1175	5	79	74	77	27	28.2
11	-	15	0.015	1225	4	11	7	9	200	263

*Includes internal upper crustal internal heating from radioactivity 4.4 by ago.

5.5 *Details of the distribution of crustal thickness and tidal dissipation*

While the tidal dissipation distribution is predominantly degree-2 in shape (see below for a quantification of this effect), it also contains a weaker degree-4 harmonic which manifests itself in the crustal thickness distribution (Fig. 2, Fig. S3, Fig. S10). In addition, there is a weak pole-to-equator surface temperature (insolation) effect. The surface temperature effect leads to thicker crust at the colder poles, and thinner crust at the hotter equator, but it is relatively minor if the tidal dissipation is strong. In Fig. S11 we show P_2 fits to swaths of the model crustal thickness (a = 20 R_E, e = 0.02, T_b = 1175 °C, q_o = 27 mW/m^2) to show their similarity to a P_2 function as a function of azimuth. The swaths are all centered at (0°, 180°E). The azimuths were chosen to capture the diversity in the crustal thickness variation, and two of the swaths (swaths M1 and M2, black and blue, respectively) are averages over large areas (θ = 90°, swaths M3-7 use θ = 10°). Swaths M1-M7 use values φ = 0°, -45°, -5°, 25°, 40°, 55°, and 85°, respectively. Least squares regressions to a P_2 function were performed from ψ = 0° to ψ = 90°.

In a similar manner to Fig. S11, we plot in Fig. S12 the dissipation distribution at the base of the crust in arbitrary units. The dissipation distribution will be approximately the same for arbitrary shell thicknesses and tidal parameters (for low e), and excludes the surface temperature effect.

While all swaths in both figures have a strong degree-2 component, in the basal dissipation distribution, only in swath M2, which is an average over azimuths 0-90° (comparable to swath 5 in Fig. 1), and in swath M5, which is an average over azimuths 40-50°, is the shape exactly degree-2. The degree-2 character of these same swaths in the crustal thickness model is also strong, but a slightly poorer match. Swath M6 in the crustal thickness model (Fig. S11) is the closest match to a perfect degree-2 shape. In all other swaths there is interference caused by the degree-4 harmonic. Least squares regression shows that swaths are entirely described by a P_2 + P_4 function (not shown). As discussed in the main text, there is evidence for the degree-4 harmonic at the terrain labeled X in Fig. 2, S3, and S10.

The relative content of degree-2 and degree-4 harmonics can be quantified by expanding the crustal thickness distribution in spherical harmonics. Taking the strongly dissipative case of $a = 20R_E$, $e = 0.02$, $T_b = 1225$ °C, $q_o = 30$ mW/m^2, we find the ratio of the sum of the squares of the degree-2 terms to the sum of the squares of the degree-4 terms is 11.9. This high ratio indicates that the degree-2 terms dominate.

Interestingly, the degree-4 harmonic averages out over azimuths 0° and 90°, as indicated by the exact P_2 fit in swath M2 (an average over azimuths 0-90°, less so in Fig. S11). This could plausibly take place if the Moon experienced a reorientation about its anti and sub-Earth points, as discussed for Europa in (*S36*).

In the absence of strong tidal heating, the equilibrium crustal thickness will follow a pattern established by the surface temperature, which varies as a function of latitude. The shape of the temperature distribution follows a $\sin^{1/4}(x)$ distribution that is very different from the crustal thickness observations (e.g. see figure 5 of (*S26*) for a plot of temperature vs. latitude), and therefore we can rule it out as describing the observations.

In general, comparison between model crustal thicknesses and dissipation distributions, and the actual data are complicated by the possibility that the Moon has reoriented itself slightly, or possibly by a large amount about the minimum moment of inertia axis that intersects the anti and sub-Earth points, such that the relationship between azimuths on the present surface and paleo-azimuths when the crust formed, is uncertain.

Ultimately, some process must have effected changes in crustal thickness either at the same time as tidally-linked crust formation, or at some later time, such that the degree-2 pattern is not observed globally (main text). There is some evidence for regionally thicker crust near the antipode of the DTT center, but this is speculative.

5.6 *Local spherical harmonic fits to the DTT*

In Fig. 2, S3, and S10 we compared profiles of the lunar crustal thickness in the DTT with the analogous profiles through a crustal thickness model predicted from tidal heating. Another means of assessing the general agreement between the tidal heating model and observations is to locally fit degree-2 spherical harmonics to the DTT and the analogous region in the tidal heating model.

We determined the best fit degree-2 spherical harmonic coefficients for the DTT by performing a least squares regression in equal-area Cartesian space over a sector from the north pole to points (-10° S, 145° E), and (-10° S, 285° E) (70° of longitude on either side of the approximate DTT center), as shown in Fig. S13a. In Fig. S13 we have shifted the lunar crustal thickness map 35° west to align the center of the DTT with the putative paleo sub and anti-Earth longitudes. The same degree-2 fit was performed for the tidal heating model, Fig. 13b. The resulting global expansions from the locally best-fit coefficients are shown in Fig. S13c and d.

In comparing Fig. S13c and 13d it is clear that the inferred degree-2 structure of the DTT is similar to what would be expected for a tidally produced terrain. Note that the local fit in part B cannot reproduce the model data exactly because the model contains higher order harmonics (predominantly degree-4).

In Table S4 we show the coefficients derived in each case. In looking at the coefficients themselves, their signs and the ratios between them determine the shapes of the expansions, and are more important than the absolute values (although they are of the same magnitude in both cases). Notably, the signs of all *C* coefficients are the same in both cases. We also find that the ratio of C_{22}/C_{21} is different by only 21% between the two cases, which is remarkably similar. The relative power of $C_{2,0}$ is higher in the model case. This results in a C_{22}/C_{20} ratio that is 70% different between the two cases, which is still fairly similar given the asymmetric state of preservation of the DTT. Note the minor *S* coefficient power reflects a slight tilt in the DTT.

Table S4. Best-fit degree-2 spherical harmonic coefficients in the DTT (map shifted 35° west)

Lunar crustal thickness coefficients (km)			**Tidal model crustal thickness coefficients (km)**		
l,m	$C_{l,m}$	$S_{l,m}$	*l,m*	$C_{l,m}$	$S_{l,m}$
2, 0	-8.2	0	2, 0	-10.3	0
2, 1	7.4	3.3	2, 1	4.3	0
2, 2	9.2	0.5	2 ,2	6.8	0

Note: *l* = degree and *m* = order.

5.7 *Effect of a low viscosity compacting layer or partially molten region at the base of the crust*

Zones of partially molten rock are predicted to occur and have been observed at the roof and base of cooling magma chambers (*S37-39*). These zones may slowly compact over time due to the weight or buoyancy of the rock matrix, squeezing out interstitial liquid as it deforms. Partially molten compacting zones may have a viscosity that is an order of magnitude smaller than for solid rock (*S40, 41*). Such a low viscosity zone at the base of the lunar crust would increase tidal dissipation there, and thereby lead to larger tidally induced crustal thickness differences for the same values of *e, a*, and T_b. This compaction process may have occurred in the lower lunar crust (*S42*), but the full details of the process have yet to be established, and for now we conservatively ignore this effect.

6. Effect of lower crustal flow on maintaining degree-2 crustal thickness differences

For non-Newtonian materials, the time τ for isostatically compensated crustal thickness differences to decay via lower crustal flow is given by ((*S43*), Appendix A)

$$\tau \approx (\Delta D^{n-1} j^{n+1} n V \delta^{n+2} E_b [g \Delta \rho_{cm}]^n)^{-1} \qquad (8)$$

Here ΔD is the initial crustal thickness contrast, j is the wavenumber of the variation, n is the exponent in the stress-strain rate relationship, $E_b = \exp(-Q/RT_b)$, and V and Q are rheological parameters (Table S2), R is the gas constant, T_b is the temperature at the base of the crust, g is the gravitational acceleration, $\Delta\rho_{cm}$ is the crust-mantle density contrast, assumed here to be 400 kg/m^3, δ is the effective thickness of the region in which channel flow occurs and a constant of order unity has been omitted. This equation reduces to the standard equation for lower crustal

flow for Newtonian materials (n = 1). Numerical models show that this expression underestimates the time taken for lower crustal flow to occur (*S43*). The effective channel thickness δ is given by

$$\delta = \frac{RT_b^2 D_m}{Q(T_b - T_s)} \quad (9)$$

where T_s is the surface temperature and D_m is the mean crustal thickness. This expression assumes that the temperature profile near the base of the crust is linear. If internal heating is important within the crust, δ will be larger and flow will be more rapid

For the parameter values summarized in Table S2, $\delta = 0.023D_m$. The wavenumber is $j = 2/R_s$ for a degree-2 variation, where R_s is the lunar radius. Taking an initial crustal thickness variation ΔD = 40 km, equation 8 gives a relaxation time of 150 by for a mean crustal thickness of 60 km, and T_b = 1175 °C. A lower T_b, which would be expected after cooling of the lithosphere, would lead to much longer relaxation times. For example, if T_b = 1000 °C, the relaxation time is ~10^5 by. Even if δ were larger than given by the linear assumption, degree-two crustal thickness variations are likely capable of surviving for 4.4 by.

A possible explanation for the lack of a more prominent degree-4 harmonic in the observed crustal thickness profiles is that limited lower crustal flow may have occurred, similar to that apparently responsible for the relaxation of some lunar basins (*S44*). Neglecting the effect of elastic support, channel flow of this kind removes short-wavelength (high frequency) topography most rapidly (*S45*), potentially allowing the longest-wavelength features to persist. Using the above parameters, T_b = 1175 °C, and $j = 4/R_s$, we obtain a relaxation time of 10 by, closer to the age of the Moon, albeit using a relatively high basal temperature during all of the flow.

7. Instability of an asymmetrical crust over a heat producing liquid layer, in the case of no convection

7.1 *Introduction*

As discussed in the main text, one of the outcomes of tidally-driven crust formation is a spatially varying thickness of the subsurface magma ocean (Fig. 3). Because the late stage magma ocean is enriched in incompatible heat producing elements, these variations in thickness will result in lateral variations of heat production. These variations will likely affect global convection patterns and crystallization processes in some manner.

If convection does not laterally transport heat efficiently and mantle topography is small, the arrangement described above and in Fig. 3 will cause higher heat flux through regions of thinner crust, and lower heat flux through regions of thicker crust, possibly amplifying (or at least maintaining) the asymmetry in crustal thickness from tides alone. Aspects of this concept have been previously articulated elsewhere (*S46-48*) to explain global lunar crustal thickness asymmetries. However, as illustrated in other studies of tidal heating in Io (*S49*), it is likely that convection will play a role in homogenizing differences in subsurface heat production. Fully resolving the behavior of this system will require numerical simulations. For example, Jupiter

has a spatially varying heat flux due to insolation, and recent 3D spherical rotating simulations of atmospheric convection have revealed complex dynamics in the distribution of heat from internal sources (*S50*).

Below we treat the problem of crustal growth over an asymmetric heat producing liquid layer, in the case of no convection. This treatment serves as simple, analytical framework that illustrates the essence of the amplification effect, and will serve as the basis for further studies that more correctly include convection.

7.2 *Instability of basal crustal topography*

If a crust becomes thick enough during growth above a heat producing layer liquid, it may become sufficiently insulating such that any further addition of crust would increase its conductive temperature profile and yield melting temperatures at its bottom, in which case its growth will cease. The thickness of a crust with no bottom topography at this time is given by:

$$D_{eq} = \frac{\Delta T_{sl} k}{q_o} \tag{10}$$

where ΔT_{sl} is the difference between the surface temperature, T_s, and the liquid temperature, T_l, k is the thermal conductivity, and q_o is the basal heat flux. We assume the basal heat flux is equal to the sum of a component due to radiogenic liquids, q_r, and a component due to cooling of the underlying mantle, q_m.

We wish to understand how asymmetries in the topography at the bottom of the growing crust will be affected by the proportional asymmetries in the height of the underlying heat-producing liquid. We assume that the total mass of heat producing elements in the liquid layer remains the same at all times of crustal growth, since the heat producing elements (K, U, and Th) are incompatible and excluded from the plagioclase (destined to float and become the crust) and pyroxene (destined to sink and become the mantle) that is crystallizing during late magma ocean cooling. We also assume that the mixing timescale for homogenization of incompatible elements across the entire magma ocean is small compared to the crystallization timescale, and therefore that the concentration of heat producing elements is the same everywhere in the ocean. This is justified given that the two relevant velocities may differ by ~10 orders of magnitude. For example, magma ocean convective velocity may be ~1 m/s (*S51*), while the late-stage crystallization front advances only ~1 m every 1000 years (given ~50 km crustal growth times of ~50 My (*S27, 28*)). We assume the change in concentration of U, Th, and K due to radioactive decay is not significant on the ~100 My timescales of crustal growth that we are interested in. We assume the mantle topography (topography at the bottom of the liquid layer) is uniform, or at least that the crustal basal topography dominates any bottom topography at long wavelengths. Again, in this treatment we also ignore lateral redistribution of heat due to convection (*S49*). The essential implication of these assumptions is that local variations in the height of the liquid layer are associated with proportional differences in the basal heat flux into the overlying crustal layer. Related aspects of this problem and the implications for the formation of the farside crust were first expressed in (*S52*).

While thicker, more radiogenic liquid layers exist under proportionately thinner crust, and thinner, less radiogenic liquid layers exist under proportionately thicker crust, the differences in basal heat flux cannot be perfectly balanced by crustal thickness differences at all locations. In fact, it can be shown that there are at most two depths at which a crust with bottom topography can be in perfect equilibrium with the basal heat flux, for any liquid layer thickness. All other locations will have crust that is too thick or thin to be in thermal equilibrium. To demonstrate this, we assume that topography perturbations *d(x)* relative to a crust of mean thickness D_{eq}, result in fractional thickness changes (1+ *d/H*) of the underlying heat producing layers, where *H* is the thickness of the liquid, measured under the crust of thickness D_{eq} (Fig. S14a and S14b). The perturbation *d* is > 0 in regions of thin crust and < 0 in regions of thick crust. Equating the equilibrium heat flux for a crust of thickness D_{eq} - *d*, and the heat delivered by the subsurface liquids of radiogenic heat flux q_r, and q_m from the cooling mantle, we have:

$$\frac{\Delta T_{sl} k}{D_{eq} - d} = q_r \left(1 + \frac{d}{H}\right) + q_m \tag{11}$$

We would like to solve for stable topography *d* as a function of *H* and D_{eq}. The above equation for *d* is quadratic and therefore there are two solutions. Using $\Delta T_{sl} k = q_o D_{eq}$, which we do throughout the remainder of this section, we have

$$\begin{aligned} d &= 0 \\ d &= D_{eq} - \frac{q_o}{q_r} H \end{aligned} \tag{12}$$

If $q_m = 0$ the nontrivial solution is $d = (D_{eq} - H)$. Essentially, subsurface topography can only be in equilibrium in two locations, which, depending on the actual, independent values of *d*, D_{eq}, and *H*, need not exist. This suggests that without convection, subsurface topography is unstable.

7.3 *Thermal equilibrium surfaces for variable basal crustal topography*

To gain insight into the behavior of basal crustal topography under these conditions, we can calculate the hypothetical equilibrium crustal thickness for a given basal topography. We model the topography perturbation *d*(*x*) a degree-2 perturbation. We again assume that at *d*(*x*) = 0 the crust is of mean thickness D_{eq}, in equilibrium with mean basal heat flux q_o, and mean liquid height *H*. As before, we assume that the perturbation *d* produces fractional thickness changes (1+ *d/H*) of the underlying heat producing layers, and proportional changes to the basal heat flux:

$$\frac{D_{eq} q_o}{D'_{eq}} = q_r \left(1 + \frac{d}{H}\right) + q_m \tag{13}$$

where D'_{eq} is a hypothetical crustal thickness that can be thicker or thinner than the actual crustal thickness D_{eq} - *d*, depending on the value of *H*. D'_{eq} represents the direction in which the crustal topography will grow or shrink due to an excess or deficit of basal heat flux.

Two different regimes of instability exist, leading to growth or decay of initial crustal topography, depending on H. These two regimes are illustrated in Fig. S14b, where we plot D'_{eq} for degree-2 basal crustal topography for two values of H. The exact H that separates the two regimes is given by the value of H that produces thermal equilibrium at the thinnest portion of the crust:

$$H_c = \frac{q_r}{q_o}(D_{eq} - d_{o,i}) \tag{14}$$

where $d_{o,i}$ is the maximum initial amplitude of the topography perturbation. For $H = H_c$, all regions of low crustal thickness ($< D_{eq}$) have $D'_{eq} \leq D_{eq} - d$, and tend to become thinner, and all regions of high crustal thickness ($> D_{eq}$) have $D'_{eq} > D_{eq} - d$, and tend to become thicker. Figure S14c shows a plot of D'_{eq} for $H = H_c$.

The critical H_c can be easily understood in the case of no constant background heating, $q_m = 0$, such that, $q_o = q_r$. Then for $d << D_{eq}$ we have $H_c \approx D_{eq}$. In this case small differences in topography yield differences in heat flux that are approximately equal to the amount of heat required for the crust to sustain a perturbation d from D_{eq}. However, if $H << D_{eq}$, the liquid concentration of heat producing elements is relatively high, and small differences in topography yield a much larger fractional change of basal radiogenic heat than needed to maintain the perturbation d relative to D_{eq}. Similarly, if $H >> D_{eq}$, the liquid concentration of heat producing elements is relatively low, and small differences in topography are associated with relatively minor changes in basal radiogenic heat, and the perturbation d cannot be sustained.

8. Final crystallization of liquids under the thin and thick regions of crust

Ultimately, whatever the final source of heat loss for the liquids that remain under the crust, they will crystallize a mixture of plagioclase and mafic minerals. Since only the plagioclase component builds the crust, the crust will only grow by a fraction of the remaining space available. This fraction will be the fraction of plagioclase crystallized from magma ocean liquids, f_p. Assuming one portion of the crust does not crystallize much more rapidly than the other, the added thickness of the plagioclase crust under the thinnest portion of the crust due to cooling is then approximately:

$$\Delta D^{thin}_{cool,plag} = f_p(H + d_o) \tag{15}$$

where d_o is the final amplitude of the degree-2 crustal thickness from tidal dissipation (Fig. S15). The added thickness of crust under the thickest portion of the crust due to cooling is similarly:

$$\Delta D^{thick}_{cool,plag} = f_p(H - d_o) \tag{16}$$

The final crustal thicknesses are therefore approximately:

$$D^{thin}_{final} = D_o - d_o + f_p(H + d_o)$$

$$D_{final}^{thick} = D_o + d_o + f_p(H - d_o) \quad (17)$$

where D_o is the mean crustal thickness. The last half of anorthositic crust formation takes place during the latest stages of magma ocean crystallization (> 90%), and the value of f_p at this time is ≈ 0.35 (*S53*). The above relationships are used to derive the final Moho surface in Fig. S15 with f_p = 0.35.

Ultimately, a mechanism for the final loss of heat is required to effect crystallization, since there are a number of geologic constraints that suggest that a liquid layer could not have existed for extensive periods of time (reviewed in (*S48, 54*)). Volcanism is an example of such a mechanism.

9. Thermal properties of the crust, mantle, and magma ocean

9.1 *Thermal properties of the crust and mantle*

For the anorthositic crust we use a thermal conductivity of 1.8 W m^{-1} K^{-1}. This value comes from the average of the conductivity for feldspar rich plutonic rocks, including anorthosite, over the temperature range of 200-750 °C (*S55*). The conductivity of these rocks decreases as a function of temperature up to ~500 C°C, but is nearly constant at 1.6 W m^{-1} K^{-1} between 500 and 750 °C. Higher temperature data could not be located. Birch and Clark (*S56*) reported anorthosite conductivity of 1.7-1.8 W m^{-1} K^{-1} at 0 °C, and an *increase* in conductivity by 9% at 300 °C. Clauser and Huenges (*S55*) interpreted the near constancy of high temperature conductivity in feldspar-rich rocks as a balance between an increasing anorthite conductivity and a decreasing mafic component conductivity. However, in light of the uncertainty of the mafic mineral content of the lunar crust, and the uncertainty in the conductivity values at temperatures above 750 °C, we use the 1.8 W m^{-1} K^{-1} estimate for the entire crust. If the conductivity does in fact increase at higher temperatures (and depth) in the Moon, this is still a fair estimate given that we are not accounting for the 5-10 fold decrease in conductivity in the 2-4 km thick surficial megaregolith, which would at least partially offset such an increase (*S57*).

For the lunar mantle and lithosphere, we use a thermal conductivity of 1.6 W/m/K. This value comes from the average of the conductivity for conduction transport dominated (vs. radiative dominated) volcanic rocks, including basalt, over the temperature range of 500-1200 °C (*S55*). The conductivity of these rocks decreases as a function of temperature up to 1200 °C. The 1.6 W m^{-1} K^{-1} estimate compares favorably with the temperature dependent conductivity as parameterized by (*S58*): 1.6 W m^{-1} K^{-1} for basic rocks (basalt), and 1.5 W m^{-1} K^{-1} for ultra basic rocks (dunite, peridotite), at a temperature of 1200 °C.

The temperature dependence of the heat capacity, *c*, of magmatic rocks, including basalts, was reported by (*S59*) and (*S60*). The temperature dependence of the heat capacity of anorthite was reported by (*S61*). In all cases, heat capacity increases with temperature. Based on these studies, a value of 1100 J kg^{-1} K^{-1} is a reasonable approximation for both basaltic rock and anorthite at temperatures above ~750 °C, and we use this value in our calculations of mantle heat flow.

Below 750 °C, ~1000 J kg^{-1} K^{-1} is a better estimate for both anorthite and basalt. For the lithosphere and crust, a value of 1000 J kg^{-1} K^{-1} is used, since average crustal and lithospheric temperatures will be lower than those of the mantle alone.

The density of the crust and mantle are assumed to be 2900 kg/m^3 and 3300 kg/m^3, respectively. The density of the lithosphere is assumed to be 3200 kg/m^3. The thermal diffusivity with the above parameters is then 6.2×10^{-7} m^2/s for the crust, 4.4×10^{-7} m^2/s for the mantle, and 5.6×10^{-7} for the lithosphere.

Relevant parameters are summarized in Table S5.

9.2 *Temperature of the magma ocean*

The magma ocean temperature is important for constraining both the viscosity of the base of the lower crust (Section 5) and the equilibrium thickness of the crust. A number of magma ocean and bulk lunar composition models have been developed to estimate the temperature as the magma ocean cooled. In the bulk Moon composition crystallization experiments of (*S62*), plagioclase first appeared at 1270 °C, suggesting this is an upper limit on the temperature just after the crust started forming. The magma ocean temperature towards the end of crustal growth can be constrained based on the liquidus and solidus of late-stage cumulates and the upper lunar mantle. The solidus of late stage Ti-rich cumulates at 100 km depth was estimated to be ~1125 °C by (*S63*). The solidus and liquidus temperature of KREEP basalt was estimated to be 1025 °C and 1175 °C, respectively (*S64*). The mantle solidus at a depth of 60 km was estimated to be 1180 °C in (*S65*). Based on these estimates, in the tidal heating calculations we assume a temperature of 1175 °C when the Moon was at 20 R_E, and 40-60 km of crust had crystallized. Note that KREEP basalt may not have yet been crystallizing when tidal dissipation was most effective.

In order to remain a fractionally crystallizing and differentiating magma ocean, the crystal fraction must be below approximately ~50% to avoid "lock up" (*S29*), and therefore the magma ocean temperature must be approximately greater than the mean temperature of the solidus and liquidus temperature of the last crystallization products. Therefore, a reasonable lower limit of final magma ocean liquid temperatures would be between the solidus and liquidus of KREEP basalt, or approximately 1100 °C.

10. Early heat flux in the magma ocean

10.1 *Introduction to a first order model*

The early lunar heat flux and heat sources determine the thickness at which the growing crust will reach conductive equilibrium. The heat flux and heat sources are important parameters in determining the equilibrium thickness for the case of an additional tidal heating source (Section 5).

Our goal in the following analysis is not to make a complete and precise model of the history of the lunar heat flux, but rather to derive reasonable estimates of relevant heat flow values from

first order assumptions informed by our recent understanding of the Moon's structure and geochemistry. Some of our assumptions are simplifications of complex and still incompletely understood processes. However, the analysis will show it is likely that during crustal growth there was a significant heat flux from radiogenic residual magma ocean liquids and cooling of the underlying mantle. Our model of the early Moon starts with a crust grown by a significant amount ~20-100 my after accretion (*S27, 28*), but assumes the crust formation process is not 100% complete.

For the sake of transparency and consistency, in our calculations we often use more decimal places than are justified given our uncertainty in the model parameters. Figure S16 will be useful in interpreting the analysis.

10.2 *Bulk radioactive element concentrations constrained by heat flow and sample chemistry*

The most important radioactive elements in the early lunar heat budget were ^{235}U, ^{238}U, ^{232}Th, and ^{40}K (*S48, 66*). A number of models for the radioactive element content of the Moon have been put forward, mostly informed by trace element abundances in lunar samples (*S67*), surface heat flow measurements (*S68*), and orbital measurements of thorium (*S69*). As in previous studies (*S66, 68*), we use the Apollo 15 and 17 heat flow measurements and the observed ratios of U, Th, and K in lunar samples as critical constraints on the bulk heat production in the Moon. We assume that the Th and U abundances are defined by the ratio Th/U = 3.70 (*S70*). This ratio is comparable to the Th/U ratio of 3.63 for chondritic meteorites (Table S5), and similar to the values used in previous work (3.8 in (*S67*), 3.7 in (*S68*), 3.5 in (*S71*)). The lunar K/U ratio was parameterized in (*S70*) to be 397Th + 154 ppm (or 1469U + 154 ppm using Th/U = 3.7), but the ratio is more variable than the Th/U ratio. The parameterization was developed based largely on high Th samples (>0.5 ppm), and leads to anomalously high K values when low Th values (< 0.2 ppm) are used as a constraint, which is the case when considering bulk Moon models. Therefore, we adopt the approximation K = 2000 × U, as in (*S66, 68, 71*) (K/U = 2066 in (*S67*) and K/U = 2500 in (*S52*)). The past heat flux for typical K, Th, and U concentrations in radiogenic magma ocean residual liquids using K = 2000 × U is less than 5% different from the value using the parameterization in (*S70*). Given these ratios of K, Th, and U, we will compare the U content of the Moon with the U content of chondritic meteorites. The past heat production, *A*, based on the present day concentration of these elements is given by equation 4.8 of (*S25*).

The measured heat flux of the Moon at the Apollo 15 and 17 sites is 21 and 14 mW/m^2, respectively, after corrections for local topography (*S68*). However, it has long been recognized that the Apollo 15 measurement is in a region of enhanced radioactivity, now known as the Procellarum KREEP Terrane (PKT) (*S72*), and that the values at the Apollo 17 site are likely closer to background values (*S68, 73*). Modeling based on megaregolith conductivity and thickness at the Apollo 17 site suggests the heat flow there is closer to 12 mW/m^2 (*S73*). More recent global data have also revealed that the Apollo 17 site is just on the edge of the PKT terrain, and may also reflect a value slightly higher than the background value, which may be ~11 mW/m^2 (*S74*).

We may estimate the mean global heat flux by accounting for the total surface area of the PKT and the Apollo 15 heat flux measured within it. The PKT occupies about 16% of the lunar

surface (*S72*). If we assume the non-PKT background heat flux is close to the mega-regolith corrected Apollo 17 value of ~12 mW/m^2 (*S73*), and a representative value for the PKT is ~21 mW/m^2, then we have:

Present global heat flux accounting for high PKT radioactivity = (0.16)21 + (0.84)12 = 13.44 mW/m^2.

This value is lower than the global 18 mW/m^2 estimate by Langesth et al. (*S68*). Depending on assumptions, it is possible the maximum heat flux in the PKT may be ~30 mW/m^2 (*S74*). Using 30 mW/m^2 instead of 21 mW/m^2 would increase the global estimate by ~2 mW/m^2.

10.3 *Observed heat flow corrected for lithosphere cooling*

The above global heat flux is not likely representative of the integrated radiogenic element heat flux because the Moon's initial heat is being lost through cooling of the lithosphere. Assuming that the first flotation crust formed at ~1200 °C (*S62*) and the surface lunar temperature is 0 °C, we may estimate the present surface heat flux from the lithosphere as the cooling of an infinite half-space over 4.4 by: $\Delta T k/\sqrt{\pi \kappa t}$, where ΔT is the difference between the initial rock temperature and the constant surface temperature (*S25*). This yields 4.36 mW/m^2, using the thermophysical properties described in Section 9.1. This assumes the upper layers cooled largely by conduction, which is a reasonable approximation given the early development of the lunar lithosphere (*S75*), and its likely monotonic growth over longer timescales (*S76*). Similar calculations are routinely applied to the oceanic lithosphere. Therefore, the theoretical global mean heat flux allowing for cooling of the lithosphere is:

Estimated present measurable global mean heat flux minus lithosphere cooling = 13.44 – 4.36 = 9.1 mW/m^2

The megaregolith in the upper ~5% of the crust may have a conductivity 5-10 times lower than the crust (*S57, 73*). However, even assuming one tenth the conductivity for the *entire* crust, (k = 0.18) the heat flux is still an appreciable 1.5 W/m^2, due to the appearance of k in both the denominator and numerator, since $\kappa = k/c\rho$. Langseth et al. (*S77*) estimated the contribution of initial heat as 2-4 mW/m^2 for 3 by of cooling, and dismissed it as negligible, compared to initially high Apollo 15 and Apollo 17 heat flux measurements of 33 mW/m^2 (*S77*) and 28 mW/m^2 (*S68, 78*), respectively (subsequently both refined downwards (*S68*)). However, in light of recently lower global mean heat flux estimates, it is relatively important.

10.4 *Unobserved extra heat flow due to radioactivity in the deep Moon*

The above refined estimate does not likely represent the total integrated radiogenic heat flux because the Moon is not likely in a steady state equilibrium with all of its heat sources, as assumed in (*S68*) and discussed in (*S73, 79*). This is because the thermal diffusion thickness $\sqrt{\kappa t}$ for 4.4 billion-year-long-cooling of the lithosphere is only ~280 km, and any radiogenic heat from beneath this level since accretion will not be observed at the surface (a point also made by (*S80, 81*)), assuming the uppermost layers of the Moon have largely cooled by conduction for most of their history. Again, this is at least a plausible first order assumption since the Moon

developed a lithosphere at an early time (*S75*). Ultimately, the depth of melting in the magma ocean determines how much of the Moon is able to upwardly concentrate U, Th, and K in the late stage liquids near the surface, which are therefore visible to surface heat flux measurements (*S82*), and how much of the deeper Moon is possibly less depleted in U, Th, and K, and invisible to heat flux measurements.

The exact depth of the magma ocean is unknown, but nearly all modern estimates are > 280 km (*S48*), such that thermal diffusion of any radiogenic heat from beneath this layer would not reach the surface in 4.4 by. Seismic data are suggestive of a discontinuity at ~500 km which may represent the depth of melting, but a melting depth of 1000 km cannot be ruled out (*S48, 83-86*). Thermal cooling and contraction models suggest a depth of ~630 km is permitted (*S87*), while petrologic constraints place limits from 450 – 1200 km (*S48, 88-91*). Hess and Parmentier (*S92*) assumed an ocean 800 km deep in their modeling of cumulate overturn and volcanism. An ocean of such a depth would produce a global anorthositic crust ~60 km thick in their model. More recent refinements of crustal thickness suggest global means of ~45-50 km (*S2, 93, 94*). Herein, we assume the depth of melting to be 600 km, which under the model of (*S92*) would lead to an average crust 45 km thick. In this case the underlying primitive mantle comprises 28% of the lunar volume. The rest of the volume would have upwardly concentrated heat producing elements into a late-stage residuum, which lies within ~75 km of the surface (*S52*). This means that 72% of the lunar radioactive elements are near the surface, which is in agreement with the 75% estimate of (*S72*). To better estimate the bulk lunar abundances of radiogenic elements, we must therefore accommodate the hypothetical heat flux (0.28/.72) × 9.1 = 3.5 mW/m^2, which would be due to deep radioactivity if it could be measured at the surface:

Theoretical present global radiogenic heat flux including deep mantle radioactivity = 9.1 + 3.5 = 12.6 mW/m^2

In making the above calculation, we have assumed that most of the radioactive elements in the primitive mantle below 600 km have not migrated upwards above the conductive cooling limit of 280 km, where they would be visible to the Apollo heat probes. While the primitive mantle would have heated and likely melted due to its heat producing element content, it is not likely that *all* of the radiogenic material would have migrated upwards above 280 km. For example, (*S76*) and (*S95*) considered the thermal evolution of the Moon with a bulk Moon U concentration of 0.030 ppm U, and 0.033 ppm U, respectively. While the internal distribution of U, Th, and K in their models was somewhat different from the one assumed here, the models found melting in the range of 300-700 km depth, which is below 280 km. Furthermore, the Moon's 500 km seismic discontinuity suggests that any level of melting and differentiation in the primitive mantle was incomplete and did not completely homogenize itself with the magma ocean cumulates (see also Section 10.8). Therefore, whatever the complex history of the primitive material from 600-1748 km depth, a reasonable first order estimate is that it did not differentiate completely such that all of its heat producing elements migrated to within the 280 km threshold required for visibility to the Apollo heat probes.

10.5 *Final corrections to observed heat flux*

A third, but less important correction to the heat flux is the lag time between the decay of radioactive elements and the time to diffuse their heat upwards. The Moon's late-stage residuum and crust should contain most of the magma ocean's radioactive elements, and are within ~75 km of the surface (*S52, 96*). The thermal diffusion time for this thickness is ~400 million years. Since this time, the present bulk lunar radioactive element concentration has decreased slightly, and we are now witnessing past heat from higher abundances of radioactive elements. However, the correction based on equation 4.8 of (*S25*) is only a difference of about 6%, which we ignore here. We also assume in this section that the concentration of radioactive elements between 75 and 280 km is negligibly low due to differentiation, which is admittedly a first order simplification.

While the uncertainty in the representative observable mean global heat flux is probably comparable to or even greater than the corrections from the above effects, we still feel the corrections are reasonable estimates, and are important in obtaining an accurate picture of the total concentrations of radioactive elements. We will use 12.6 mW/m^2 as our model-derived hypothetical present heat flux due to the all of the Moon's radioactivity.

We find that assuming U abundances of 0.032 ppm (equivalent to 4.0 × chondritic values, Table S5), the U/Th and U/K ratios discussed above, a bulk lunar density of 3340 kg/m^3, and a radius of 1737.4 km, we obtain a present hypothetical global heat flux from all radioactive sources of 12.6 mW/m^2. As a check of our calculations, if we assume a present U concentration of 0.046 ppm, as in Langseth et al. (*S68*), we obtain a heat flow of 18.0 mW/m^2, in agreement with Langseth et al. (*S68*). Drake (*S97*) and Hood (*S98*) estimated that mean heat flow measurements of 11 and 14 mW/m^2 would be in equilibrium with bulk U of 0.029 and 0.033 ppm, respectively.

The bulk U concentration for this model is similar to Taylor's (*S99*) estimate of 0.033 ppm and Joliff's et al.'s (*S72*) more recent estimate of 0.039 ppm. Drake (*S97, 100*) estimated U concentrations of 0.020 ppm for a 50 km thick crust assuming no U remained in the mantle. Assuming that 28% of the Moon retained its primitive U conentration, as we have, would make his estimate 0.029 ppm, which is also close to ours. Wieczorek and Phillips (*S74*) found a bulk U abundance of 0.024 ppm would be consistent with heat flux observations at the Apollo 15 and 17 sites. Rasmussen and Warren (*S57, 73*) estimated lower U concentrations of ~0.020 ppm based on a number of assumptions about regolith properties and lunar geotherms.

The U concentration for our model and the several others cited are larger than the estimated silicate Earth concentration of ~0.020 ppm (*S101*). The reason why the Moon appears to have a greater abundance of heat producing elements than the silicate Earth from which it was presumably largely derived is not clear, but it is the outcome of a number of models. Wieczorek et al. (*S2*) point out that an enriched abundance of Th (and thereby U) would be consistent with a Moon enriched in aluminum. Table S5 gives a summary of the estimated abundances for U, K, and Th in chondrites, the Earth, and our lunar model.

Using U = 4.0 × chondritic values abundances (U = 0.032 ppm), and allowing for the decay of radioactive isotopes over 4.4 by, we have during the early magma ocean epoch:

Hypothetical global heat flux from all U, Th, and K radioactivity 4.4 by ago = 43.0 mW/m^2

In the following sections, we will refine how this integrated heat flux was distributed in the mantle, crust, and late-stage liquids on the early Moon.

10.6 *Primitive mantle contribution to early radiogenic heat production*

As discussed in Section 10.4, the depth of the lunar magma ocean determines how much of the radioactive element budget is incorporated into the crust and late stage liquids, and how much remains in the primitive interior. Assuming again a magma ocean depth of 600 km, 28% of the bulk lunar U, Th, and K cannot completely migrate upwards during differentiation. Therefore, assuming the mode of heat transport is conduction, the contribution of these elements to the heat flux at the base of the early lunar crust is 0.28 × 43.0 = 12.0 mW/m^2, and can be subtracted from the heat flux due to radioactivity from the bulk Moon:

Past global radiogenic heat flux minus deep primitive mantle radioactivity = 43.0 -12.0 = 31.0 mW/m^2

This decrease in basal heat flux at the crust will lead to a larger crustal thickness in equilibrium with subsurface heat.

The same reasoning used in Section 10.4 can be applied here to argue that the primitive mantle did not necessarily release all of its radiogenic elements to within the thermal diffusion depth necessary to affect the early basal crustal heat flux. In this case, the relevant thermal diffusion time is the time of near-completion of magma ocean crystallization, about 100 my, which has a diffusion depth of only 40 km in the mantle. It is unlikely the sub-600-km-deep primitive mantle would have differentiated fully and all of its radioactive elements would have migrated upwards to within 40 km of the base of the crust, within 100 my. Therefore, the above correction is reasonable to first order.

Table S5. Lunar heat flux model parameters

Radioactive element parameter	**U**	**^{232}Th**	**K**
Chondritic abundances*, ppm	0.008	0.029	550
Silicate Earth abundances, ppm (*S101*)	0.020	0.80	240
Assumed present lunar abundances†, ppm	0.032	0.118	64
Half lives, years (*S25*)	7.04×10^8 (^{235}U), 4.47×10^9 (^{238}U)	1.4×10^{10}	1.25×10^9 (^{40}K)
Heat production, *A*, W kg^{-1} (*S25*)	5.69×10^{-4} (^{235}U), 9.46×10^{-5} (^{238}U)	2.64×10^{-5}	2.92×10^{-5} (^{40}K)
Model parameters		**Value‡**	
Derived present global mean heat flux, mW m^{-2}		13.4	
Present heat flux from lithosphere cooling, mW m^{-2}		4.4	
Present deep (unseen) radiogenic heat flux, mW m^{-2}		3.5	
Present total radiogenic heat flux, mW m^{-2}		12.6	
Model bulk Moon radiogenic heat flux 4.4 by ago, mW m^{-2}		43.0	
Past radiogenic heat flux from upper crust, mW m^{-2}		10.9	
Past deep radiogenic heat flux, mW m^{-2}		12.0	
Past radiogenic heat flux from magma ocean liquids, mW m^{-2}		21.1	
Past heat flux from mantle cooling, mW m^{-2}		7.3	
Conductivity of the crust, W m^{-1} K^{-1}		1.8	
Conductivity of the mantle, W m^{-1} K^{-1}		1.6	
Heat capacity of the mantle alone, J kg^{-1} K^{-1}		1100	
Heat capacity of the crust and lithosphere, J kg^{-1} K^{-1}		1000	
Crust density, kg m^{-3}		2900	
Lithosphere density, kg m^{-3}		3200	
Mantle density, kg m^{-3}		3300	
Bulk Moon density, kg m^{-3}		3340	
Crust thermal diffusivity, m^2 s^{-1}		6.2×10^{-7}	
Lithosphere thermal diffusivity, m^2 s^{-1}		4.4×10^{-7}	
Mantle thermal diffusivity, m^2 s^{-1}		5.6×10^{-7}	

* Chondritic abundances from the range reported in (*S101*).

† Assuming U = 0.032, Th/U = 3.70, K/U = 2000.

‡ Heat flow values are reported with one decimal place accuracy only for transparency in the calculations.

10.7 *Heat production from elements in the early (and present) upper crust*

The partitioning of Th, U, and K between the crust and residual liquids is important for constraining the equilibrium crustal thickness during magma ocean crystallization. While most incompatible elements should be trapped in late-stage liquids sandwiched between the crust and mantle, remote sensing data suggests significant upper crustal abundances of thorium compared to the bulk Moon (*S72*). Warren et al. (*S102*) inferred that bulk crustal abundances were ~1-1.7 ppm, and that thorium decreases with increasing depth. Langseth et al. (*S68*) and Metzger et al. (*S69*) also assumed bulk crustal thorium of ~1 ppm. The plausible origins of this surface enhancement likely include incorporated melt in flotation cumulates (*S42*), excavation and remobilization of KREEPy intrusive rocks such as the Mg-suite (see page 385 of (*S48*)), and possibly global redistribution of KREEP-rich Imbrium ejecta (*S103*). Which effect dominates is unknown, but the fact that thorium is not symmetric across the highlands (*S103*) suggests global melt trapping in the first few kilometers of crust is not the entire explanation. Further, thorium's negative correlation with crustal thickness (*S102*) is evidence that post-magma ocean intrusive processes may be important.

Regardless of the exact mechanism of surface enhancement, it is unlikely that the crust can be uniformly composed of ~1 ppm thorium. Firstly, such a crust would be too rich in heat

producing elements to be compatible with global differentiation and segregation of heat producing elements into a radiogenic late-stage residuum (*S52, 54*). This can be illustrated by the theoretical present day heat flux from a crust with 1 ppm Th (and 0.27 ppm U, 540 ppm K). Such a crust has a heat production of 1.6×10^{-7} W/m^3, using parameters in Table S5. For a mean crustal thickness of 45 km, the crust would have a heat flux of 7.0 mW/m^2. However, in Section 10.3 we calculated that the heat flux from shallow radioactivity after accounting for lithospheric heat is ~9 mW/m^2. Therefore, a uniform crust of 1 ppm Th would explain nearly all (75%) of the observed lunar heat flow without the existence of a significant late-stage radiogenic residuum layer (> 1 ppm thorium) at depth, which is very likely to exist in some form.

Secondarily, a crust uniform in ~1 ppm thorium ignores strong constraints imposed by the thorium concentration of the ferroan anorthosite (FAN) suite. The FAN suite is believed to form a large fraction of the lunar crust (*S96*), and extremely pure anorthosite has recently been observed globally (*S104*). Such pure anorthosite may form by efficient extrusion of trapped melt during extremely slow cooling and compaction in the mid to lower levels of the lunar crust (*S42*). Pristine FAN suite rocks typically have Th concentrations between 0.01 and 0.1 ppm (e.g. Fig. 3b of (*S105*), Fig. 3.4 of (*S2*), discussion in (*S70*) and (*S52*)), usually more than an *order of magnitude smaller* than assumed for bulk crustal models. For example, the well-studied pristine FAN 15415 "Genesis Rock" (*S106*) has a Th concentration of 0.003-0.028 (*S107-109*), and FANs 60025 and 67075 also have very low Th concentrations of 0.0002-0.005 ppm (*S110*) and 0.015-0.046 ppm (*S111-113*), respectively. Notably, 60025 and 67075 likely formed at depths of ~21 and ~14 km, respectively, based on cooling rate estimates (*S114*). Because the FAN suite is believed to form a large fraction of the lunar crust, it is unlikely that the 1 ppm thorium values observed near the surface with gamma ray spectroscopy are representative of the crustal thorium more than a couple tens of kilometers depth. McCallum et al. (*S114*) also concluded that there was a reduced KREEPy signature in the middle crust, and that rocks from the lower half of the crust have probably not been sampled. A more reasonable alternative to a uniform thorium content in the crust is that thorium decreases with depth, plausibly due to increasing efficiency of extrusion of radiogenic KREEP-rich liquids from crustal rocks as the crustal growth rate slows, as suggested by (*S42*).

To account for a decrease in thorium with depth, and the observation of ~1 ppm levels in the upper crust, we assume an exponential decrease in thorium and volumetric heat production, A, with depth, D, as is common for models of Earth's crust,

$$A(D) = A_o e^{-D/D_r} \tag{18}$$

where A_o is the surface heat production rate and D_r is a spatial decay constant. The temperature associated with a layer of thickness D with exponentially decreasing heat production is (*S25*)

$$\Delta T = \frac{A_o D_r^2}{k}\left(1 - e^{-D/D_r}\right) \tag{19}$$

The surface heat flux from exponentially decreasing heat production in a crust of infinite depth is (*S25*)

$$q = A_o D_r \tag{20}$$

We assume that that the present near-surface concentration is 1 ppm thorium (and 0.27 ppm U, 540 ppm K), yielding a heat production of:

A_o =1.6 ×10^{-7} W/m^3, today,
A_o = 5.4 ×10^{-7} W/m^3, 4.4 by ago.

Warren et al. (*S102*) estimated ~ 1 ppm thorium crustal abundances from materials exposed by excavation of the upper ~25 km of crust. We assume:

D_r = 20 km.

This depth is also consistent with the very low Th values of anorthosites 60025 and 67075, believed to be derived from 14-21 km depth. This results in a 4.4-by-old surface heat flux due to upper crustal radioactivity:

Past radiogenic global heat flux from upper crustal radioactivity alone = 10.9 mW/m^2,

assuming an infinite depth crust. This is a good approximation if $D > 2D_r$, since the heat production drops by a factor of $1\text{-}1/e^2 = 0.86$ in this distance. Since this is usually the case in the crust, we can subtract this crustal heat flux from the non-primitive-mantle radiogenic heat flux to obtain the contribution from the subsurface radiogenic residual liquids alone:

Past radiogenic global heat flux due residual radiogenic liquids alone = 31.0 – 10.9 = 20.1 mW/m^2

This calculation implicitly assumes that crustal thorium was trapped in the crust immediately as it formed, not by some post-crust formation process that brought it from depth, as discussed above. If this is not the case, then the past radiogenic heat flux from subsurface liquids would be greater.

The above calculation also assumes the abundance of radioactive elements in upper mantle cumulates is negligible. This assumption is difficult to assess because many of the lunar samples derived from the mantle have interacted with the KREEP-rich region near the crustal boundary. As discussed by (*S115*), mare basalts may incorporate KREEP through assimilation, contamination during passage to the surface, or during downwelling of KREEP rich material into the mantle. Similar processes may have operated for the volcanic glasses (*S116*). Until better information becomes available, our first order approximation is that the magma ocean portion of the differentiated mantle sequestered a negligible amount of heat producing elements compared to the crust.

For the inferred *present* Th abundances, the exponentially decreasing heat production model gives a present crustal surface heat flux of 3.2 mW/m^2, which is 35% of the inferred 9.1 mW/m^2 total radiogenic heat flux. If the non-crustal non-primitive-mantle abundances of Th, U, and K in this model were entirely trapped in a late-stage global 5-km-thick layer 50 km deep, the present

abundances would be 10.5 ppm Th, 2.8 ppm U, and 5670 ppm K, which is within the range observed in KREEP basalts (e.g (*S70*)).

10.8 *Contribution of upper mantle cooling to early heat flux*

As plagioclase floats in the magma ocean to form the lunar crust, mafic minerals co-crystallize and sink to form the lunar mantle. These denser cumulates overlie hotter, earlier cumulates that vary in temperature up to 1600 °C (*S62*). The cooling of these cumulates will release heat into the overlying liquid layer, thereby adding to the basal heat flux into the crust from radioactivity. This added heat flux will alter the crustal thickness that will be in equilibrium with subsurface heat. Whether heat from these early cumulates was transported by conduction or convection is unknown, but as reviewed extensively on pages 475-480 of (*S48*), there are a number of reasons why conduction may have been the dominant mode of heat transport. For example, the upward-growing cumulate mantle became progressively denser with crystallization, such that it would be stable against convection (*S92, 117*). Even if convection developed in the lunar mantle, the onset of convection may have been delayed for hundreds of millions of years (*S118*), such that it may not be relevant to the basal heat flux during final crystallization of the overlying crust. Eventually, in the very final stages of magma ocean crystallization, we do not rule out an overturn event due to density differences (*S54*).

Assuming conductive heat transport from underlying cumulates is a reasonable first order approximation, it is not trivial to calculate the heat flux since cooler cumulates are continually being added to the hotter underlying cumulates and continually insulating them. Furthermore, the liquid temperature at the surface of the cumulates is continually decreasing as the magma ocean crystallizes. However, an estimate of the heat flux may be calculated by assuming that a mass of cumulates formed at some initial temperature, and has ever since been cooling to the temperature of the late-stage liquids. This allows the cooling to be modeled by cooling of a semi-infinite half space, as in Section 10.3. If we assume an upper mantle cumulate temperature of 1450 °C, and a temperature of 1150 °C for the late stage liquids, we then have a heat flux of

Early mantle cooling contribution to basal heat flux: 7.3 mW/m^2.

Therefore, the approximate heat flux at the base of the early-forming crust is:

Past global radiogenic heat flux minus mantle radioactivity, plus cumulate cooling = 20.1 + 7.3 = 27.4 mW/m^2
(Final estimate of early basal crustal heat flux)

To summarize, we have an ancient basal crustal heat flux of 27.3 mW/m^2, which is the sum of components from radiogenic liquids (20.1 mW/m^2) and mantle cooling (7.3 mW/m^2). A component due to radiogenic elements in the upper crust (10.9 mW/m^2) and the deep, primitive mantle (12.1 mW/m^2) have been subtracted from the global flux heat budget. To obtain these estimates, a deep primitive mantle radiogenic heat production was added to the observed lunar heat flux, and a lithosphere cooling component was subtracted. This process and our assumptions are summarized in Fig. S16.

11. Comments on the possibility of other processes in creating degree-2 geologic signatures

Other geophysical processes that are associated with long wavelength perturbations include convection and Rayleigh-Taylor instabilities, for either liquids or solids. The role of these processes has been implicated in creating north-south crustal thickness changes on Mars (*S119, 120*), and nearside-farside compositional anomalies on the Moon (*S121*). However, just because a process can be explained mathematically by low-order spherical harmonics, or that process has length scales comparable to the low-order harmonics of interest, it does not mean that the process will precisely create a geologic terrain with the same spherical harmonic *shape*. For example, neither the Mars crustal thickness distribution (*S122*) nor the lunar nearside compositional anomaly (the PKT) follow precisely degree-1 shapes, as the DTT does for degree-2, despite their prevalence in one hemisphere. In the case of mantle convection, a further difficulty is that the physical mechanism by which crustal thickness differences can be created is not well established (*S120*). The possible role of long-lived mantle convection in the Moon in creating the DTT is also diminished by the apparent very early development of the DTT, inferred from its general state of isostasy (main text, SOM Section 3). Therefore, we conclude that with the current information available, tidal dissipation processes, which have a well-established means of producing dominantly degree-2 crustal thickness differences (*S20-22*) (Section 5.5), as observed in the DTT, are a more plausible explanation for the DTT.

12. Further investigation of the Mare Oceanus and Mare Frigoris border

To further investigate the relationship between DTT crustal thickness and topography at the border of Oceanus Procellarum and Mare Frigoris, we plot in Fig. S17a and S17b the topography and crustal thickness along these units' borders, as defined by the red line in Fig. 1a and 1c. We also plot the free air anomaly from Kaguya SGM100h (Fig S17c).

In all three datasets the standard deviations along the border are 3 to 6 times lower than the standard deviations for the global datasets, even though the border profiles trace a distance of ~6000 km, equivalent to about half the lunar circumference. As an example, the topography standard deviation is only 340 m over this range, compared to 2130 m globally. There is also little, if any, long wavelength trend in any of the border traces. In other words, the crustal thickness, topography, and gravity are rather constant along the border. A similar trend in topography referenced to the geoid is discernable from figure 1 of (*S123*).

We have argued elsewhere that the crustal thickness in this region is a part of the DTT, and the DTT is an ancient province created during crust formation (age 4.5-4.3 Ga), prior to extrusion of nearside mare basalts (ages < 3.9 Ga, volcanism duration > 1 billion years (*S124*)). Therefore, this constancy of the crustal thickness suggests that the Mare Frigoris and Oceanus Procellarum borders, and ultimately the northern and western volcanic limits of the PKT, are controlled by pre-existing crustal thicknesses variations established by the DTT. This relationship does not establish when the PKT radiogenic anomaly was created (for example, either coeval with or after DTT formation). However, it does suggest that the significant mantle melting and volcanism associated with the PKT took place after DTT formation, and therefore these events had the potential to modify the preexisting terrain closer to the PKT center, perhaps resulting in the lack of obvious present day degree-2 structure in the central PKT.

SOM References

S1. Smith, D.E. and M.T. Zuber. Inferences about the early Moon from gravity and topography, in *Origin of the Earth and Moon Conference* (1998). Houston, TX: Lunar and Planetary Institute.

S2. Wieczorek, M.A., et al., The constitution and structure of the lunar interior, *Rev. Mineral. Geochem.* **60**, 221-364 (2006).

S3. Wieczorek, M.A. and R.J. Phillips, Potential anomalies on a sphere: applications to the thickness of the lunar crust, *J. Geophy. Res.* **103**, 1715-1724 (1998).

S4. Namiki, N., et al., Farside Gravity Field of the Moon from Four-Way Doppler Measurements of SELENE (Kaguya), *Science* **323**, 900-905 (2009).

S5. Ishihara, Y., et al., Crustal thickness of the Moon: Implications for farside basin structures, *Geophys. Res. Lett.* **36**, L19202 (2009).

S6. Khan, A. and K. Mosegaard, An inquiry into the lunar interior: A nonlinear inversion of the Apollo lunar seismic data, *J. Geophy. Res.* **107**, 3-1 (2002).

S7. Lognonne, P., J. Gagnepain-Beyneix, and H. Chenet, A new seismic model for the Moon: Implications for structure, thermal evolution and formation of the Moon, *Earth and Planetary Science Letters* **211**, 27-44 (2003).

S8. Jeffreys, H., *The Earth* (1976), Cambridge: Cambridge University Press.

S9. Lambeck, K. and S. Pullan, The lunar fossil bulge hypothesis revisited, *Physics of the Earth and Planetary Interiors* **22**, 29-35 (1980).

S10. Smith, D.E., et al., Topography of the Moon from the Clementine LIDAR, *J. Geophy. Res.* **102**, 1591 (1997).

S11. De Hon, R.A., Thickness of the western mare basalts, *Proc. Lunar Sci. Conf. 10th*, 2935-2955 (1979).

S12. Heather, D.J. and S.K. Dunkin, A stratigraphic study of southern Oceanus Procellarum using Clementine multispectral data, *Planetary and Space Science* **50**, 1299-1309 (2002).

S13. Whitford-Stark, J.L., The volcanotectonic evolution of Mare Frigoris, *Proc. Lunar Sci. Conf. 20th*, 175-185 (1990).

S14. Hiesinger, H., et al., Ages and stratigraphy of lunar mare basalts in Mare Frigoris and other nearside maria based on crater size-frequency distribution measurements, *J. Geophy. Res.* **115**, E03003 (2010).

S15. Kaula, W.M.S., G.; Lingenfelter, R. E.; Sjogren, W. L.; Wollenhaupt, W. R., Apollo laser altimetry and inferences as to lunar structure, *Proc. Lunar Sci. Conf. 5th*, 3049-3058 (1974).

S16. Murray, C.D. and S.F. Dermott, *Solar system dynamics* (2001), Cambridge: Cambridge University Press.

S17. Kaula, W.M., *An introduction to planetary physics* (1968), New York: John Wiley & Sons, In.c.

S18. Ray, R.D., R.J. Eanes, and F.G. Lemoine, Constraints on energy dissipation in the Earth's body tide from satellite tracking and altimetry, *Geophysical Journal International* **144**, 471-480 (2001).

S19. Peale, S.J. and P. Cassen, Contribution of tidal dissipation to lunar thermal history, *Icarus* **36**, 245-269 (1978).

S20. Nimmo, F., et al., The global shape of Europa: Constraints on lateral shell thickness variations, *Icarus* **191**, 183-192 (2007).
S21. Ojakangas, G.W. and D. Stevenson, Thermal state of an ice shell on Europa, *Icarus* **81**, 220-241 (1989).
S22. Tobie, G., A. Mocquet, and C. Sotin, Tidal dissipation within large icy satellites: Applications to Europa and Titan *Icarus* **177**, 534-549 (2005).
S23. Tobie, G., G. Choblet, and C. Sotin, Tidally heated convection: Constraints on Europa's ice shell thickness, *J. Geophy. Res.* **108**, 5124 (2003).
S24. Rybacki, E. and G. Dresen, Dislocation and diffusion creep of synthetic anorthite aggregates, *J. Geophy. Res.* **105**, 26,017-26,036 (2000).
S25. Turcotte, D.L. and G. Schubert, *Geodynamics* (2001): Cambridge University Press. 528.
S26. Vasavada, A.R., D.A. Paige, and S.E. Wood, Near-Surface Temperatures on Mercury and the Moon and the Stability of Polar Ice Deposits, *Icarus* **141**, 179-193 (1999).
S27. Solomon, S.C. and J. Longhi, Magma oceanography: 1. Thermal evolution, *Proc. Lunar Sci. Conf. 8th*, 583-599 (1977).
S28. Nemchin, A., et al., Timing of crystallization of the lunar magma ocean constrained by the oldest zircon, *Nature geoscience* **2**, 133-136 (2009).
S29. Tonks, B. and H.J. Melosh, *The physics of crystal settling and suspension in a turbulent magma ocean*, in *Origin of the Earth*, H. Newsom and J. Jones, Editors. 1990, Oxford U. Press. p. 151-174.
S30. Williams, J.G., et al., Lunar rotational dissipation in solid body and molten core, *J. Geophy. Res.* **106**, 27933-27968 (2001).
S31. Mignard, F., The lunar orbit revisited, III, *Moon Planets* **24**, 189-207 (1981).
S32. Walker, J.C.G. and K.J. Zahnle, Lunar nodal tide and distance to the Moon during the Precambrian, *Nature* **320**, 600-602 (1986).
S33. Touma, J. and J. Wisdom, Resonances in the early evolution of the Earth-Moon system, *The Astronomical Journal* **115**, 1653-1663 (1998).
S34. Kokubo, E., S. Ida, and J. Makino, Evolution of a circumterrestrial disk and formation of a single moon, *Icarus* **148**, 419-436 (2000).
S35. Cuk, M., Excitation of lunar eccentricity by planetary resonances, *Science* **318**, 244 (2007).
S36. Ojakangas, G.W. and D.J. stevenson, Polar wander of an ice shell on Europa, *Icarus* **81**, 242-270 (1989).
S37. Shirley, D.N., Differentiation and Compaction in the Palisades Sill, New Jersey, *J. Petrology* **28**, 835-865 (1987).
S38. Tegner, C., et al., Differentiation and Compation in the Skaergaard Instrusion, *J. Petrology* **50**, 813-840 (2009).
S39. McKenzie, D., The generation and compaction of partially molten rock, *J. of Petrology* **25**, 713-765 (1984).
S40. Hirth, G. and D.L. Kohlstedt, Experimental constraints on the dynamics of the partially molten upper mantle: Deformation in the dislocation creep regime., *J. Geophy. Res.* **100**, 15441-15449 (1995).
S41. Hirth, G. and D.L. Kohlstedt, Experimental constraints on the dynamics of the partially molten upper mantle: Deformation in the diffusion creep regime., *J. Geophy. Res.* **100**, 1981-2001 (1995).

S42. Parmentier, E.M. and Y. Liang, Formation of pure anorthosite during lunar magma ocean solidification: implications for the melt-solid segregation process, *LPSC 41st*, Abstract 1824 (2010).
S43. Nimmo, F., R.T. Pappalardo, and B. Giese, On the origins of band topography, Europa, *Icarus* **166**, 21-32 (2003).
S44. Mohit, P.S. and R.J. Phillips, Viscoelastic evolution of lunar multi-ring basins, *J. Geophy. Res.* **111**, E12001 (2006).
S45. Nimmo, F. and D. Stevenson, J., Estimates of Martian crustal thickness from viscous relaxation of topography, *J. Geophy. Res.* **106**, 5085-5098 (2001).
S46. Warren, P.H. and G.W. Kallemeyn. Pristine rocks, remote sensing, and the lunar magmasphere hypothesis, in *Workshop on New Views of the Moon* (1998). Houston, TX.
S47. Wasson, J.T. and P.H. Warren, Contribution of the mantle to the lunar asymmetry, *Icarus* **44**, 752-771 (1980).
S48. Shearer, C.K., et al., Thermal and magmatic evolution of the Moon, *Reviews in Mineralogy and Geochemistry* **60**, 365-518 (2006).
S49. Tackley, P.J., Convection in Io's asthenosphere: Redistribution of nonuniform tidal heating by mean flows, *Journal of Geophysical Research* **106**, 32,971-32,981 (2001).
S50. Aurnou, J., et al., Convective heat transfer and the pattern of thermal emission on the gas giants, *Geophysical Journal International* **173**, 793-801 (2008).
S51. Solomatov, V.S. and D.J. Stevenson, Suspension in convective layers and style of differentiation of a terrestrial magma ocean, *J. Geophy. Res.* **98**, 5375-5390 (1993).
S52. Warren, P.H. and J.T. Wasson, The origin of KREEP, *Reivews of Geophysics* **17**, 73-88 (1979).
S53. Snyder, G.A., L.A. Tayor, and C.R. Neal, A chemical model for generating the sources of mare basalts: Combined equilibrium and fractional crystallization of the lunar magmasphere, *Geochimica et Cosmochimica Acta* **56**, 3809-3823 (1992).
S54. Hess, P.C. and E.M. Parmentier, Thermal evolution of a thicker KREEP liquid layer, *J. Geophy. Res.* **106**, 28,023 - 28,032 (2001).
S55. Clauser, C. and E. Huenges, *Thermal conductivity of rocks and minerals*, in *Rock physics and phase relations: A handbook of physical constants*, T.J. Ahrens, Editor. 1995, American Geophysical Union: Washington DC.
S56. Birch, F. and H. Clark, The thermal conductivity of rocks and its dependence upon temperature and composition, *American Journal of Science* **238**, 529-558 (1940).
S57. Warren, P.H. and K.L. Rasmussen, Megaregolith insulation, internal temperatures, and bulk uranium content of the moon, *J. Geophy. Res.* **92**, 3453-3465 (1987).
S58. Zoth, G. and R. Hanel, *Appendix* in *Handbook of Terrestrial Heat-Flow Density Determination*, R. Hanel, L. Rybach, and L. Stegena, Editors. 1988, Kluwer Academic Publishers: Dordrecht.
S59. Vosteen, H.-D. and R. Schellschmidt, Influence of temperature on thermal conductivity, thermal capacity and thermal diffusivity for different types of rock, *Physics and Chemistry of the Earth, Parts A/B/C* **28**, 499-509 (2003).
S60. Bouhifd, M.A., et al., Thermochemistry and melting properties of basalt, *Contrib. Mineral. Petrol.* **153**, 689-698 (2007).
S61. Courtail, P., C. Tequi, and P. Richet, Thermodynamics of diopside, anorthite, pseudowollastonite, CaMgGeO4 olivine, and akermanite up to near the melting point, *Phys. Chem. Minerals* **27**, 245-250 (2000).

S62. Ringwood, A.E., Limits on the bulk composition of the moon, *Icarus* **28**, 325-349 (1976).
S63. Van Orman, J.A. and T.L. Grove, Origin of lunar high-titanium ultramafic glasses: Contraints from phase relations and dissoution kinetics of clinopyroxene-ilmenite cumulates, *Meteoritics & Planetary Science* **35**, 783-794 (2000).
S64. Rutherford, M.J., B. Tonks, and B. Holmberg, Experimental Study of KREEP Basalt Evolution: The Origin of QMD and Granite at the Base of the Lunar Crust, *Proc. Lunar Sci. Conf. 27th*, 1113-1114 (1996).
S65. Elkins, L.T., B.H. Hagar, and T.L. Grove, Magmatic effects of the lunar late heavy bombardment, *Earth and Planetary Science Letters* **222**, 17-27 (2004).
S66. Toksőz, M.N. and S.C. Solomon, Thermal History and Evolution of the Moon, *The Moon* **7**, 251-278 (1973).
S67. Hays, J.F., Radioactive heat sources in the lunar interior *Physics of the Earth and Planetary Interiors* **5**, 77-84 (1972).
S68. Langseth, M.G.K., S. J.; Peters, K., Revised lunar heat-flow values *Proc. Lunar Sci. Conf. 7th*, 3143-3171 (1976).
S69. Metzger, A.E., et al., Thorium concentrations in the lunar surface. I: Regional values and crustal content, *Proc. Lunar Sci. Conf. 8th*, 949-999 (1977).
S70. Korotev, R.L., Concentrations of radioactive elements in lunar materials, *J. Geophy. Res.* **103**, 1691 (1998).
S71. Toksőz, M.N. and D.H. Johnston, The evolution of the Moon, *Icarus* **21**, 389-414 (1974).
S72. Jolliff, B.L., et al., Major lunar crustal terranes: Surface expressions and crust-mantle origins, *J. Geophy. Res.* **105**, 4197-4216 (2000).
S73. Rasmussen, K.L.W., P. H., Megaregolith thickness, heat flow, and the bulk composition of the moon, *Nature* **313**, 121-124 (1985).
S74. Wieczorek, M.A. and R.J. Phillips, The "Procellarum KREEP Terrane": Implications for mare volcanism and lunar evolution, *J. Geophy. Res.* **105**, 20417-20430 (2000).
S75. Zuber, M.T., et al., The Shape and Internal Structure of the Moon from the Clementine Mission, *Science* **266**, 1839-1843 (1994).
S76. Spohn, T., et al., The longevity of lunar volcanism: implications of thermal evolution calculations with 2D and 3D mangtle convection models, *Icarus* **2001**, 54-65 (2001).
S77. Langseth, M.G., et al., The Apollo 15 lunar heat-flow measurement, *Moon* **4**, 390-410 (1972).
S78. Langseth, M.G., S.J. Keihm, and J.L. Chute, *Heat-flow experiment*, in *Apollo 17 Prelim. Sci. Rep.* 1973. p. 9-1 to 9-24.
S79. Schubert, G., D. Stevenson, and P. Cassen, Whole planet cooling and the radiogenic heat source content of the Earth and Moon, *J. Geophy. Res.* **85**, 2531-2538 (1980).
S80. Conel, J.E. and J.B. Morton, Interpretation of lunar heat flow data, *Moon* **14**, 263-289 (1975).
S81. Hanks, T.C. and D.L. Anderson, Origin, evolution and present thermal state of the Moon, *Physics of the Earth and Planetary Interiors* **5**, 409-425 (1972).
S82. Keihm, S.J. and M.G. Langseth, Lunar thermal regime to 300 KM, *Proc. Lunar Sci. Conf. 8th*, 499-514 (1977).
S83. Mueller, S., G.J. Taylor, and R.J. Phillips, Lunar composition - A geophysical and petrological synthesis, *J. Geophy. Res.* **93**, 6338-6352 (1988).

S84. Hood, L.L. and M.T. Zuber, *Recent Refinements in Geophysical Constraints on Lunar Origin and Evolution*, in *Origin of the Earth and Moon*, R.M. Canup and K. Righter, Editors. 2000, University of Arizona Press: Tucson. p. 397-409.
S85. Khan, A., K. Mosegaard, and K.L. Rasmussen, A New Seismic Velocity Model for the Moon from a Monte Carlo Inversion of the Apollo Lunar Seismic Data, *Geophys. Res. Lett.* **27**, 1591 (2000).
S86. Nakamura, Y., Seismic velocity structure of the lunar mantle, *J. Geophy. Res.* **88**, 677-686 (1983).
S87. Kirk, R.L.S., David J., The competition between thermal contraction and differentiation in the stress history of the moon, *J. Geophy. Res.* **94**, 12133-12144 (1989).
S88. Elkins-Tanton, L.T.C., N.; Grove, T. L., Experimental and petrological constraints on lunar differentiation from the Apollo 15 green picritic glasses, *Meteoritics &Planetary Science* **38**, 515-527 (2003).
S89. Barr, J.A. and T.L. Grove, Primordial Lunar Mantle Melts and Assimilated Magma Ocean Cumulates: Implications for the Depth of the Lunar Magma Ocean Based on Ultramafic Glass Compositions, *LPSC 41st*, Abstract 2427 (2010).
S90. Elkins, L.T., et al., Origin of lunar ultramafic green glasses: constraints from phase equilibrium studies, *Geochimica et Cosmochimica Acta* **64**, 2339-2350 (2000).
S91. Longhi, J., Origin of picritic green glass magmas by polybaric fractional fusion, *Proc. Lunar Sci. Conf. 22nd*, 343-353 (1992).
S92. Hess, P.C. and E.M. Parmentier, A model for the thermal and chemical evolution of the Moon's interior: implications for the onset of mare volcanism, *Earth and Planetary Science Letters* **134**, 501-514 (1995).
S93. Wieczorek, M.A., Gravity and topography of the terrestrial planets, *Treatise on Geophysics* **10**, 165-206 (2007).
S94. Hikida, H. and M.A. Wieczorek, Crustal thickness of the Moon: New constraints from gravity inversions using polyhedral shape models, *Icarus* **192**, 150-166 (2007).
S95. Ziethe, R., K. Seiferlin, and H. Hiesinger, Duration and extent of lunar volcanism: Comparison of 3D convection models to basalt ages, *Planetary and Space Science* **57**, 784-796 (2009).
S96. Warren, P.H., The magma ocean concept and lunar evolution, *Ann. Rev. Earth Planet. Sci* **13**, 201-240 (1985).
S97. Drake, M.J., *Is lunar bulk material similar to earth's mantle?*, in *Origin of the Moon*, W.K. Hartmann, R.J. Phillips, and G.J. Taylor, Editors. 1986, Lunar and Planetary Institute: Houston. p. 105-124.
S98. Hood, L.L., *Geophysical constraints on the lunar interior*, in *Origin of the Moon*, W.K. Hartmann, R.J. Phillips, and G.J. Taylor, Editors. 1986, Lunar and Planetary Institute: Houston. p. 361-410.
S99. Taylor, S.R., *Planetary science: A lunar perspective* (1982), Houston: Lunar and Planetary Institute.
S100. Drake, M.J., Geochemical Constraints on the Origin of the Moon: Abundance of U, *Meteoritics & Planetary Science* **31**, A38 (1996).
S101. McDonough, W.F. and S.-S. Sun, The composition of the Earth, *Chemical geology* **120**, 223-253 (1995).
S102. Warren, P.H., Compositional structure within the lunar crust as constrained by Lunar Prospector thorium data, *Geophys. Res. Lett.* **28**, 2565-2568 (2001).

S103. Haskin, L.A., The Imbrium impact event and the thorium distribution at the lunar highlands surface, *J. Geophy. Res.* **103**, 1679 (1998).
S104. Ohtake, M.M., Tsuneo; Haruyama, Junichi; Yokota, Yasuhiro; Morota, Tomokatsu; Honda, Chikatoshi; Ogawa, Yoshiko; Torii, Masaya; Miyamoto, Hideaki; Arai, Tomoko; et al., The global distribution of pure anorthosite on the Moon, *Nature* **461**, 236-240 (2009).
S105. Taylor, G.J., Ancient lunar crust: Origin, composition, and implications, *Elements* **5**, 17-22 (2009).
S106. Steele, I.M.S., J. V. , Mineralogy of Apollo 15415 ``Genesis Rock" : Source of Anorthosite on Moon, *Nature* **234**, 138-140 (1971).
S107. Keith, J.E., R.S. Clark, and K.A. Richardson, Gamma-ray measurements of Apollo 12, 14, and 15 lunar samples, *Proc. Lunar Sci. Conf. 2nd*, 1671-1680 (1972).
S108. Tera, F., L.A. Ray, and G.J. Wasserburg, *Distribution of Pb-U-Th in lunar anorthosite 15415 and inferences about its age*, in *The Apollo 15 Lunar Samples*, C.a. Watkins, Editor. 1972, Lunar and Planetary Institute: Houston. p. 396-401.
S109. Tatsumoto, M., et al., *U-Th-Pb, Rb-Sr, and K measurements on some Apollo 15 and Apollo 16 samples*, in *The Apollo 15 Lunar Samples*, C.a. Watkins, Editor. 1972, Lunar and Planetary Institute: Houston. p. 391 - 395.
S110. Hanan, B.B.T., G. R., 60025 - RELICT of primitive lunar crust?, *Earth and Planetary Science Letters* **84**, 15-21 (1987).
S111. Silver, L.T., Uranium-Thorium-Lead Isotopic Characteristics in some Regolithic Materials from the Descartes Region, *LPI 4th*, 672-674 (1973).
S112. Premo, W.R., M. Tatsumoto, and J.W. Wang, PB isotopes in anorthositic breccias 67075 and 62237 - A search for primitive lunar lead, *Proc. Lunar Sci. Conf. 19th*, 61-71 (1989).
S113. Hubbard, N.J.S., C.-Y.; Rhodes, J. M.; Wiesmann, H.; Bansal, B. M., The chemical definition and interpretation of rock types returned from the non-mare regions of the moon, *Proc. Lunar Sci. Conf. 5th*, 1227-1246 (1974).
S114. McCallum, I.S. and H.E. O'Brien, Stratigraphy of the lunar highland crust: Depth of burial of lunar samples from cooling-rate studies, *American Mineralogist* **81**, 1166-1175 (1996).
S115. Neal, C.R. and G.J. Taylor, Petrogenesis of mare basalts: a record of lunar volcanism, *Geochimica et Cosmochimica Acta* **56**, 2177-2211 (1992).
S116. Shearer, C.K. and J.J. Papike, Basaltic magmatism on the Moon: A perspective from volcanic picritic glass beads, *Geochimica et Cosmochimica Acta* **57**, 4785-4812 (1993).
S117. Alley, K.M. and E.M. Parmentier, Numerical experiments on thermal convection in a chemically stratified viscous fluid heated from below: implications for a model of lunar evolution, *Physics of the Earth and Planetary Interiors* **108**, 15-32 (1998).
S118. Pritchard, M.E. and D.J. Stevenson, How Has the Moon Released Its Internal Heat?, *LPSC 30th*, 1981 (1999).
S119. Roberts, J.H. and S. Zhong, Degree-1 convection in the Martian mantle and the origin of the hemispheric dichotomy, *J. Geophy. Res.* **111**, E06013 (2006).
S120. Zhong, S. and M.T. Zuber, Degree-1 mantle convection and the crustal dichotomy on Mars, *Earth and Planetary Science Letters* **189**, 75-84 (2001).
S121. Parmentier, E.M., S. Zhong, and M.T. Zuber, Gravitational differentiation due to initial chemical stratification: origin of lunar asymmetry by the creep of dense KREEP? , *Earth and Planetary Science Letters* **201**, 473-480 (2002).

S122. Andrews-Hanna, J.C., M.T. Zuber, and W.B. Banerdt, The Borealis basin and the origin of the martian crustal dichotomy, *Nature* **453**, 1212-1215 (2008).
S123. Wieczorek, M.A., M.T. Zuber, and R.J. Phillips, The role of magma buoyancy on the eruption of lunar basalts, *Earth and Planetary Science Letters* **185**, 71-83 (2001).
S124. Hiesinger, H., et al., Ages and stratigraphy of mare basalts in Oceanus Procellarum, Mare Nubium, Mare Cognitum, and Mare Insularum, *J. Geophy. Res.* **108**, 5065 (2003).

SOM Figure Captions

Figure S1

Diagram of the relevant variables for calculating great circle swaths of topography, crustal thickness, and tidal dissipation across the Moon.

Figure S2

A) Additional farside topography swaths fit to P_2, and vertically offset for clarity, as in Fig. 1a. Parameters are shown in Table S1. B) Swaths plotted over LOLA topography data (4-pixel-per-degree), as in Fig. 1b. C-D) Same as A and B but for crustal thickness.

Figure S3

Same as Fig. 2 but for the additional profiles given in Fig. S2. A) Mean profiles of lunar crustal thickness swaths derived from tidal dissipation at $a = 20\ R_E$, $e = 0.02$, $T_b = 1175$ °C, and $q_o = 27$ mW/m^2 (black lines), along with the profiles from Fig. 1c (multiplied by 0.4, blue lines, arbitrarily offset). Swath dimensions are the same as in Fig. S2. Vertical axis applies to tidal model swath 1 only, but scale is constant throughout. Fit directions are indicated, but no fits were performed in this figure. B) Map of crustal thickness used for part A. Model data in both parts have been shifted 35° east.

Figure S4

Values of R^2 for fits to a degree-2 oscillation, for points on the lunar globe separated with 2° resolution, for $\varphi = 0°$ and $\theta = 90°$, and $\psi = 105°$, in simple cylindrical projection. A) R^2 values with no contrast enhancement (min = 0, max = 0.9865). B) Values of R^2 contrasted to highlight points with $R^2 > 0.8$ (min = 0.8, max = 0.9865). Two regions of high quality fits are indicated by the two arrows. C) Values of R^2 contrasted to highlight points with $R^2 > 0.95$ (min = 0.95, max = 0.9865). The two swaths plotted in Fig. S5 are centered at the points indicated with the two arrows (-84° S, 194°E) and (78° N, 74° E).

Figure S5

A) Representative swaths of topography from the two regions of high quality fits shown in Fig. S4c. The swaths were calculated with $\varphi = 0°$, $\theta = 90°$, and $\psi = 105°$, and fit to a P_2 function. Note that both swaths start with low topography and end with high topography. B) Swaths plotted over LOLA topography data (4-pixel-per-degree). Both swaths extend into the farside highlands within the DTT region fitted to a P_2 function in the main text.

Figure S6

Same as Fig. S4a, but for $\varphi = -90°$ and $\theta = 180°$. Minimum $R^2 = 0$, maximum $R^2 = 0.9987$. The DTT stands out as a distinct island. The arcuate region of high R^2 values to the east of the DTT

is due to the low topography trough of the eastern portion of the DTT. This figure is used to help estimate the approximate center of the DTT.

Figure S7

A) Four topography swaths (#11-14) from pole to pole, together encompassing all of the nearside, and an additional swath (#15) on the farside. The swaths were fitted to a P_2 function with a maximum or minimum amplitude at the equator. B) Swaths plotted over LOLA topography data (4-pixel-per-degree).

Figure S8

A-C) P_2 and degree (n) 2, 3, and 4 polynomial ($Q_n(x)$) fits to the topography from swaths 1, 2 and 3 from the main text. Dashed lines indicated 95% confidence intervals. D-F) Same as parts A-C but for crustal thickness.

Figure S9

A and B) Best fit P_2 and P_1 (cos(x)) functions for a region very similar to swath 1 (see Section 1.7), and the unmodified swath 5, respectively, for crustal thickness data. C and D) Residuals from the fits in parts A and B, respectively. The residuals in the P_1 fits show symmetric and periodic structure, while the residuals in the P_2 fits are approximately evenly distributed about zero, suggesting that the P_2 function is much more likely to be the correct representation of the terrain than a P_1 function.

Figure S10

Same as Fig. 2 (main text) but for the higher dissipation case with T_b = 1225 °C (a = 20 R_E, e = 0.02, q_o = 30 mW/m^2).

Figure S11

A) Swaths of crustal thickness from the tidal dissipation model with T_b = 1175 °C (a = 20 R_E, e = 0.02, q_o = 27 mW/m^2), fit to a P_2 function over 90° of great circle arc. All swaths are centered at (0°N, 180° E), which is the anti-Earth point. The swaths are intended to illustrate the variation of the crustal thickness pattern with azimuth, as well as characterize the pattern's similarity to a P_2 function. B) Map of crustal thickness for the model in A.

Figure S12

Same as Fig. S11 but for a map of the basal dissipation rate, in arbitrary units of energy per unit time per unit volume.

Figure S13

Local degree-2 fits to the DTT (part A) and the analogous region in the most dissipative tidally-driven crustal thickness model considered (part B, T_b = 1225 °C, a = 20 R_E, e = 0.02, q_o = 30 mW/m^2). The resulting global expansions from the coefficients found in A and B are shown in parts C and D, respectively. The similarity of parts C and D suggest that the DTT is indeed representative of a tidally-driven crustal thickness province. See Section 5.6.

Figure S14

Amplification of late-stage basal crustal topography in the case of no lateral heat transport by ocean convection. A) The lunar crust in conductive equilibrium with basal heat flux $q_o = q_r + q_m$, and mean liquid depth H. B) Degree-2 topography on the crust-liquid interface with amplitude $d_{o,i}$. Dashed and dot-dashed lines are surfaces in equilibrium with basal heat, calculated with respect to the solid line, for $H < H_c$ and $H > H_c$. Surfaces were calculated for $d_{o,i}$:D_{eq} = 1:50. C) Crust-liquid interface with degree-2 topography of amplitude $d_{o,i}$, and mean thickness D_{eq} (solid black line). The blue dashed line is the crust-liquid surface in equilibrium with basal heat, calculated with respect to the solid line, for $H = H_c$. $H = H_c$ yields an equilibrium surface which is coincident with the thinnest crust, such that values of $H < H_c$ lead to melting of crust for all crustal thicknesses < D_{eq}, and growth of crust for all crustal thicknesses > D_{eq}. The calculation was done with a ratio d_o:D_{eq} = 1:5. A large ratio of d_o:D_{eq} is used here to illustrate the relationship of H_c to the crust-liquid interface.

Figure S15

Initial degree-2 crustal thickness differences will be reduced when the remaining subsurface liquid crystallizes, depending on the fraction of plagioclase, f_p, crystallized, and the mean depth H. In this example, the approximate final Moho topography is illustrated for f_p = 0.35, assuming one portion of the crust does not crystallize much more rapidly than the others.

Figure S16

Sources of heat in the past and present Moon. The present observed surface heat fluxes are used to derive a first order model for bulk lunar U, Th, and K, and these bulk abundances are used to construct the past heat flux model. Allowances are made for the distribution of heat producing elements in the Moon, as well as early mantle and present lithosphere cooling. Darker colors represent regions with greater amounts of U, Th, and K. The present non-mantle radiogenic heat flux and lithosphere cooling heat flux do not sum up to the inferred measurable mean surface heat flux of 13.4 mW/m^2 because their values have been rounded. Not to scale.

Figure S17

Profiles of topography (A), crustal thickness (B), and free air gravity anomaly (C) data along the Mare Frigoris and Oceanus Procellarum borders (data collected along the red line in Fig. 1a and 1c). The profiles start in the east, near (38° N, 47.5° E) at the eastern edge of Mare Frigoris, and move westward and eventually south along the Oceanus Procellarum border until (-13° S, 316°

E, rightmost portion of plot). Horizontal lines indicate mean values over the border trace. The scales of the vertical axes reflect the approximate range of most of the data observed globally for each data set. The low standard deviations and lack of any significant long-term trends indicate the border data are rather constant.

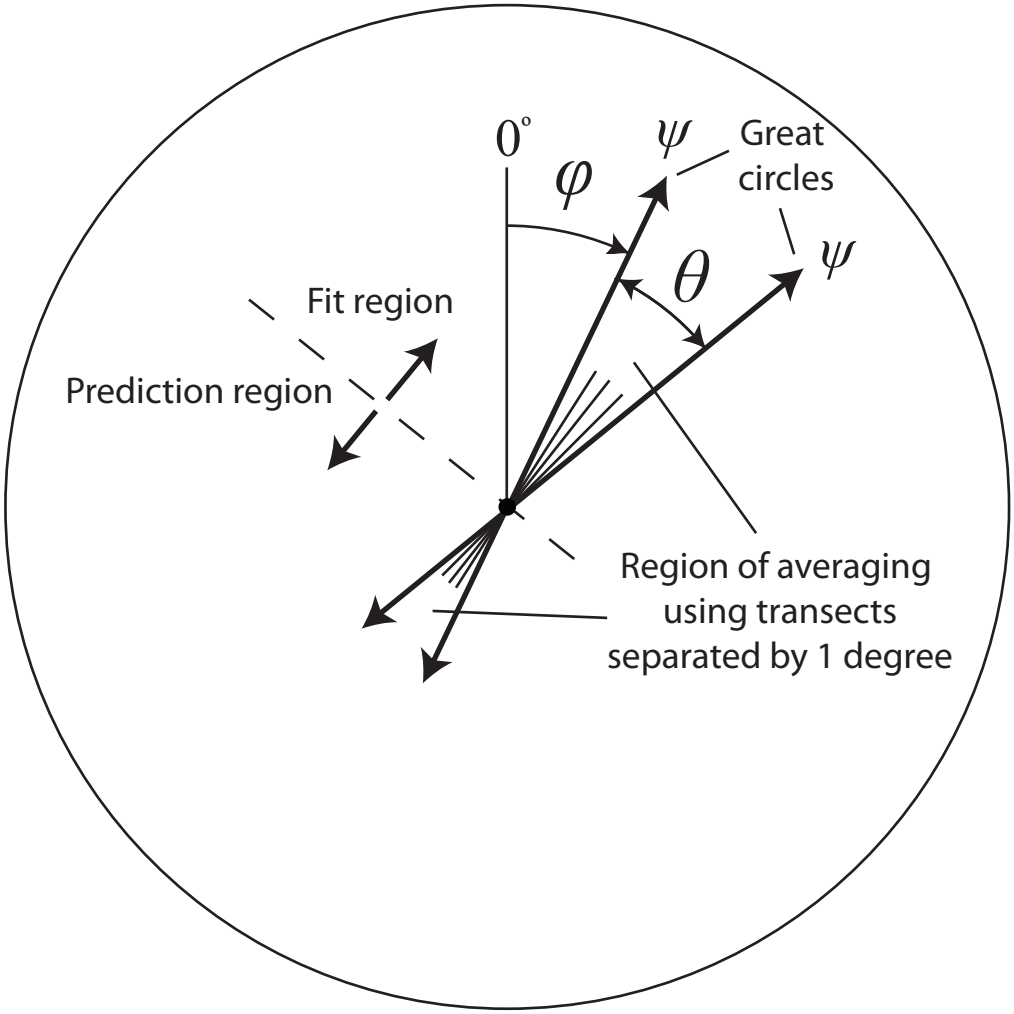
0°
φ
ψ
Great
circles
θ
ψ
Fit region
Prediction region
Region of averaging
using transects
separated by 1 degree

Figure S1

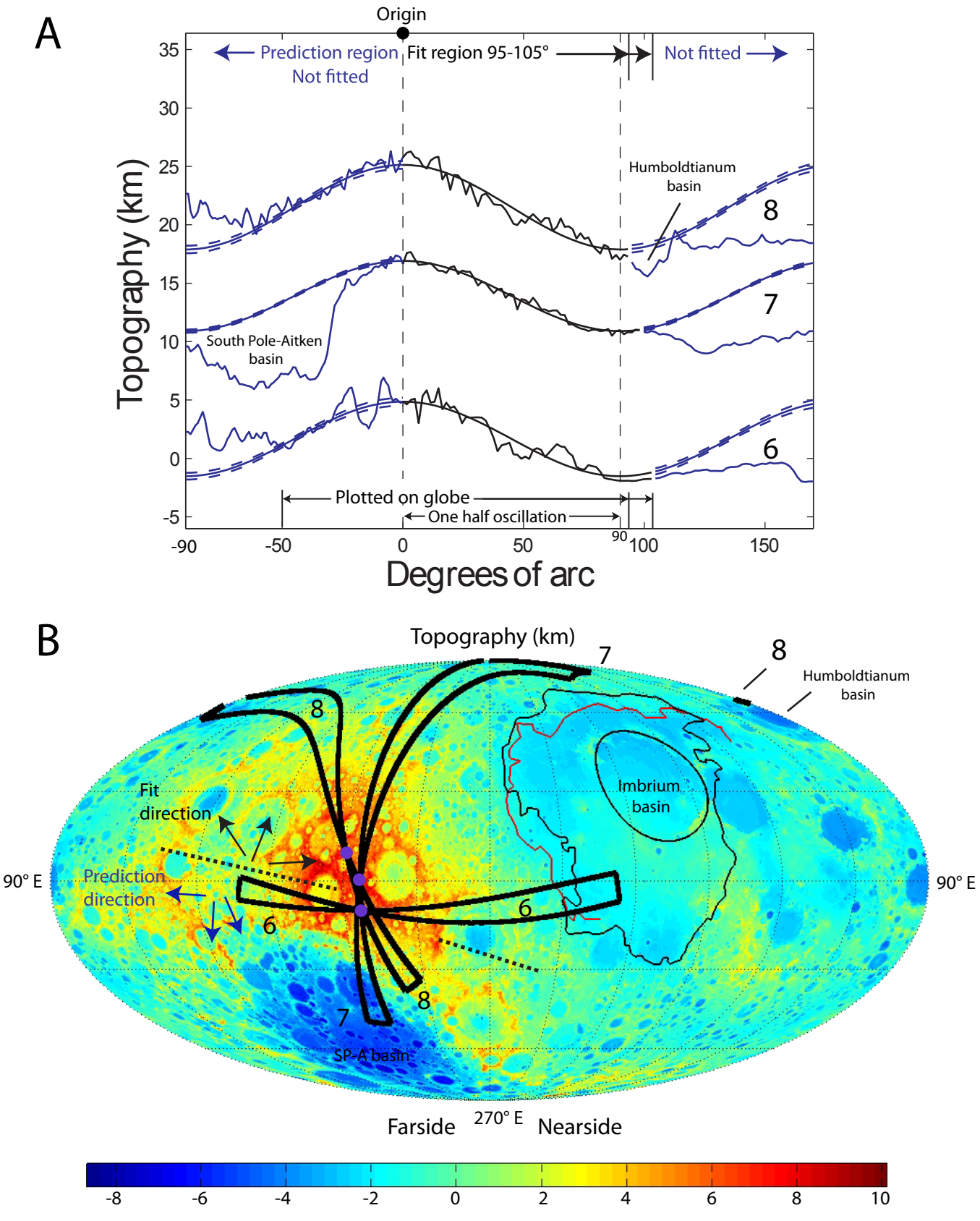

Figure S2, parts A and B

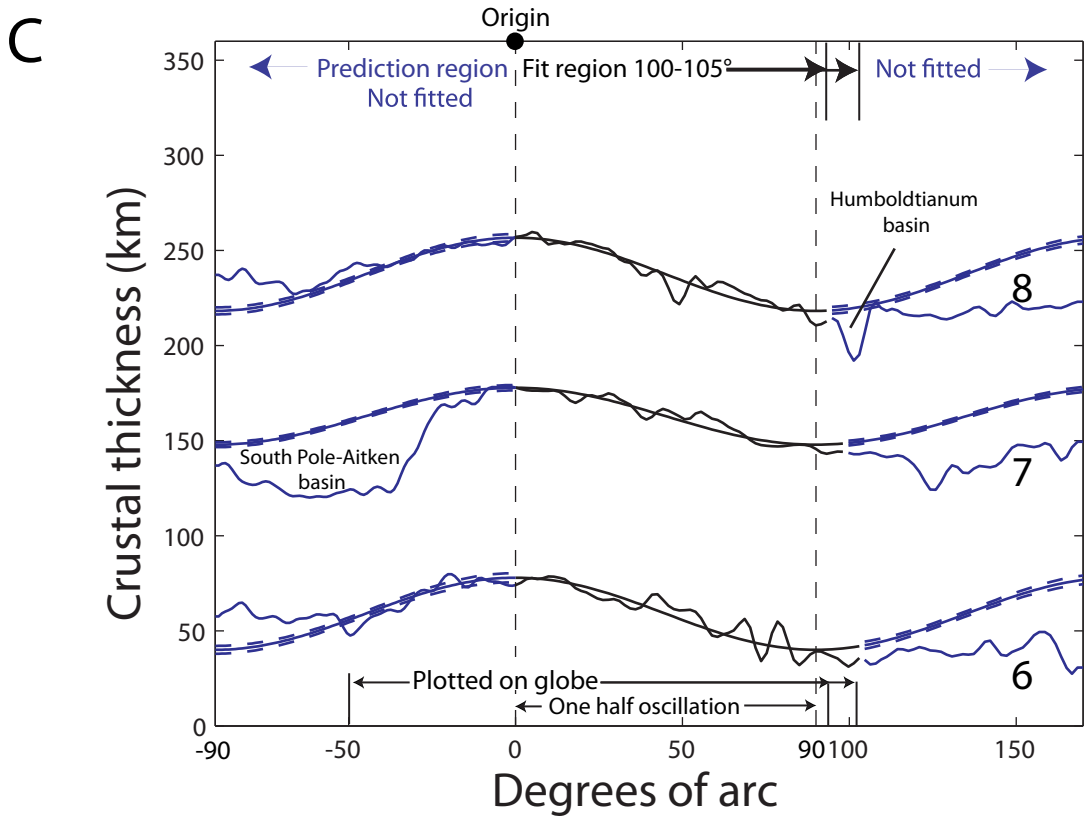

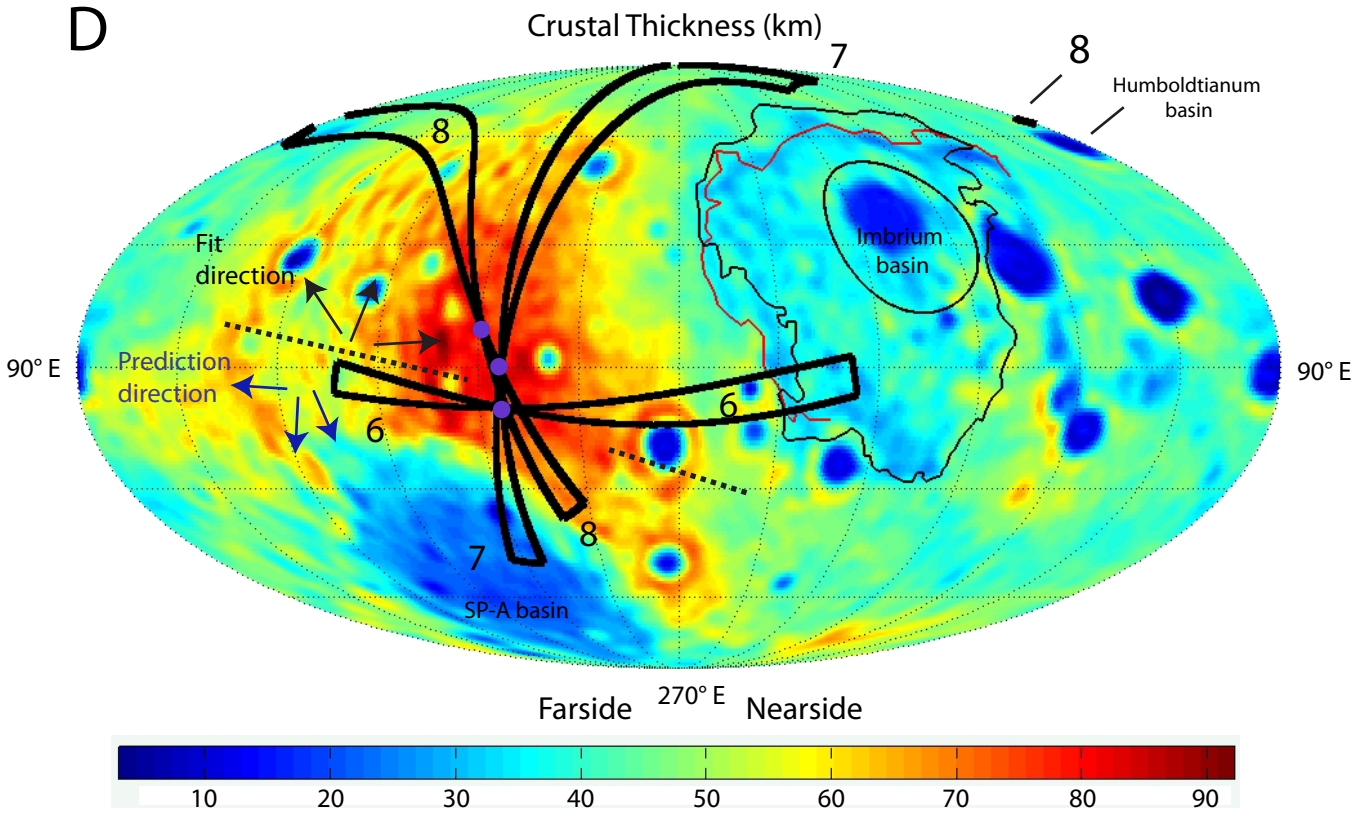

Figure S2, parts C and D

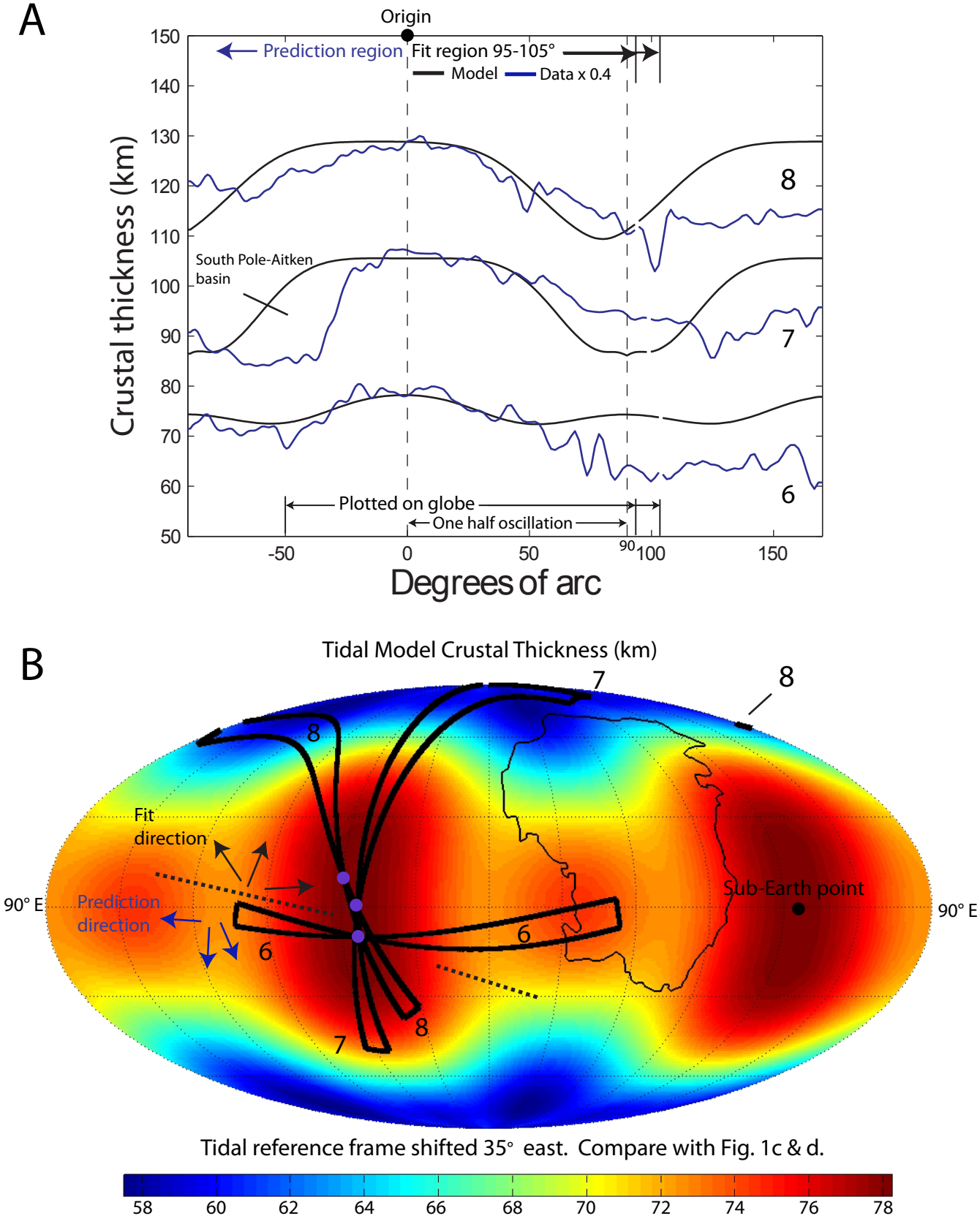
A
Origin
Prediction region
Fit region 95-105°
Model
Data x 0.4
Crustal thickness (km)
South Pole-Aitken basin
8
7
6
Plotted on globe
One half oscillation
Degrees of arc
B
Tidal Model Crustal Thickness (km)
Fit direction
Prediction direction
Sub-Earth point
90° E
90° E
Tidal reference frame shifted 35° east. Compare with Fig. 1c & d.
58 60 62 64 66 68 70 72 74 76 78

Figure S3

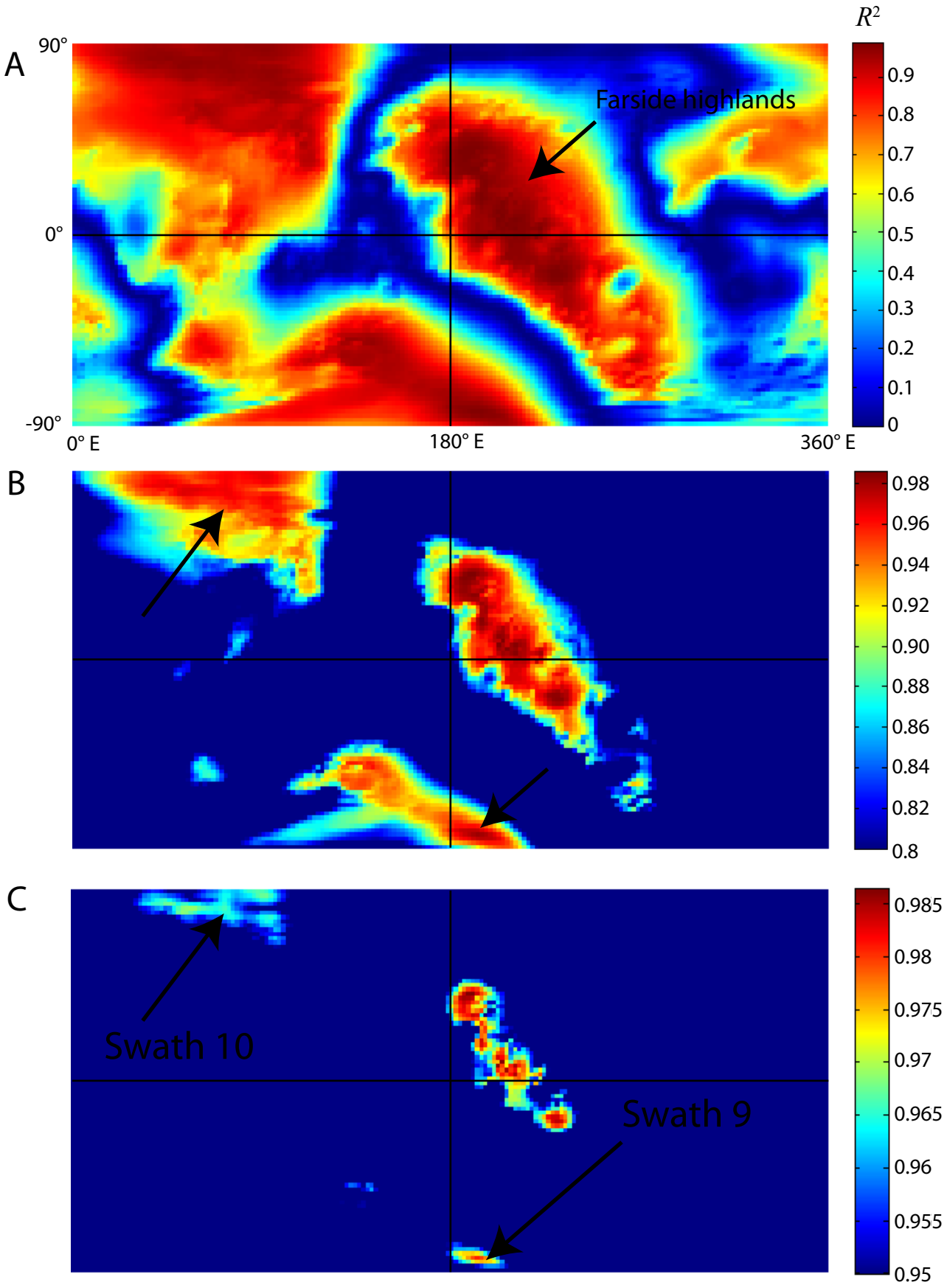
A
R^2
90°
0°
-90°
0° E
180° E
360° E
Farside highlands
0.9
0.8
0.7
0.6
0.5
0.4
0.3
0.2
0.1
0
B
0.98
0.96
0.94
0.92
0.90
0.88
0.86
0.84
0.82
0.8
C
Swath 10
Swath 9
0.985
0.98
0.975
0.97
0.965
0.96
0.955
0.95

Figure S4

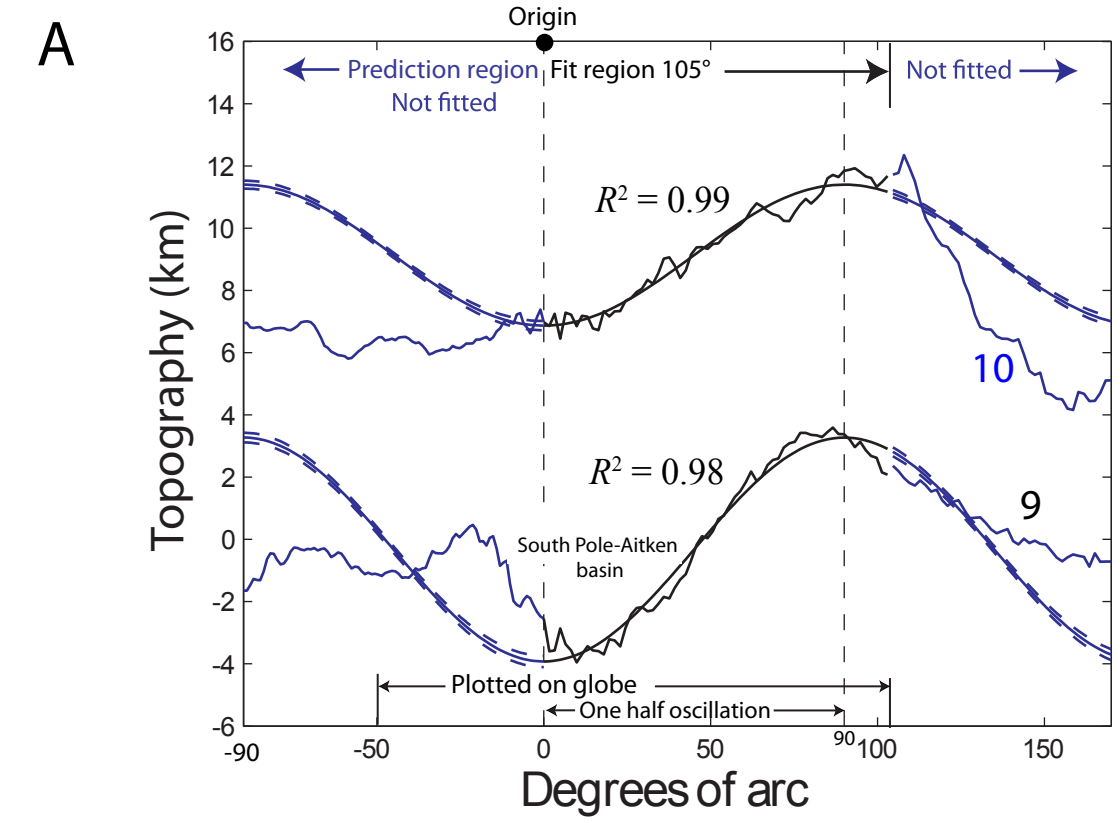
A
Origin
Prediction region
Not fitted
Fit region 105°
Not fitted
$R^2 = 0.99$
10
$R^2 = 0.98$
9
South Pole-Aitken basin
Plotted on globe
One half oscillation
Topography (km)
Degrees of arc
16
14
12
10
8
6
4
2
0
-2
-4
-6
-90
-50
0
50
90
100
150

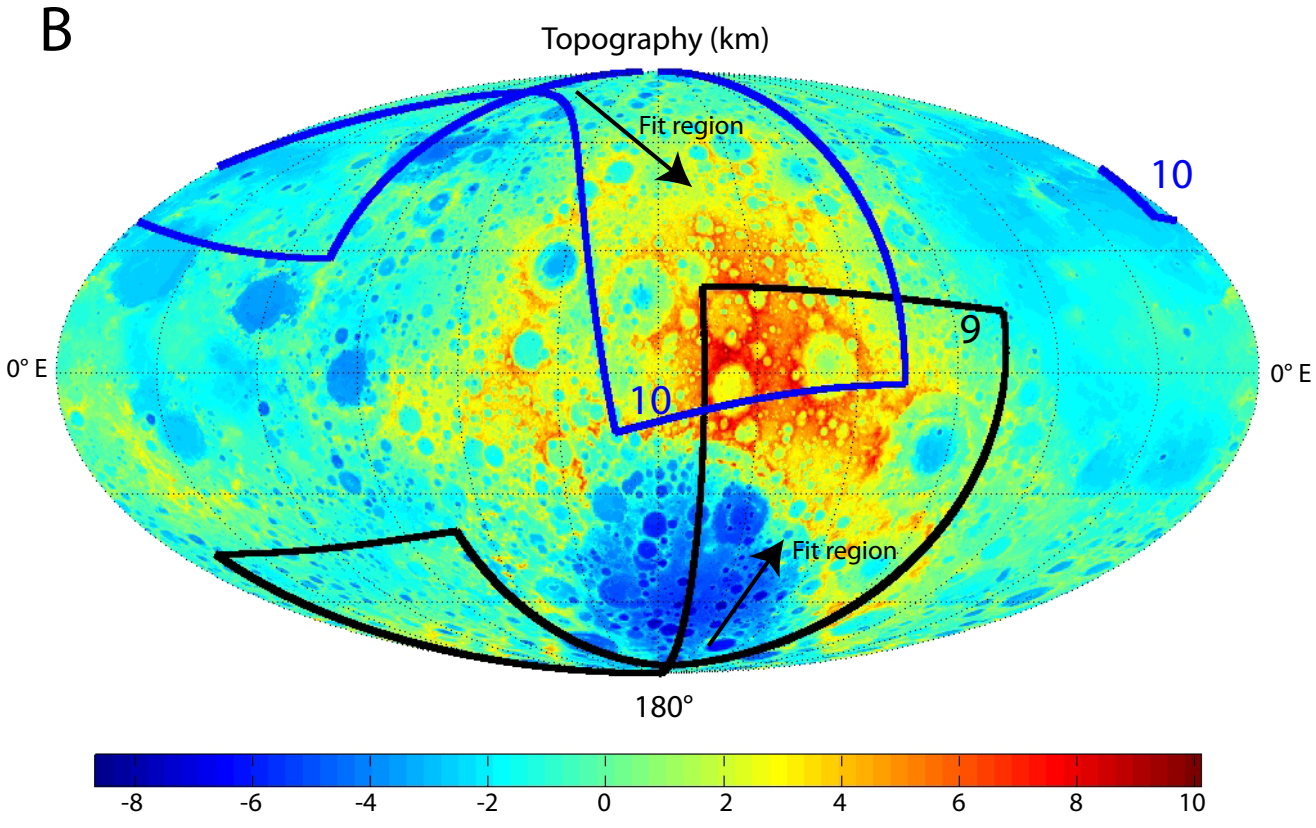
B
Topography (km)
Fit region
10
9
10
Fit region
0° E
0° E
180°
-8
-6
-4
-2
0
2
4
6
8
10

Figure S5

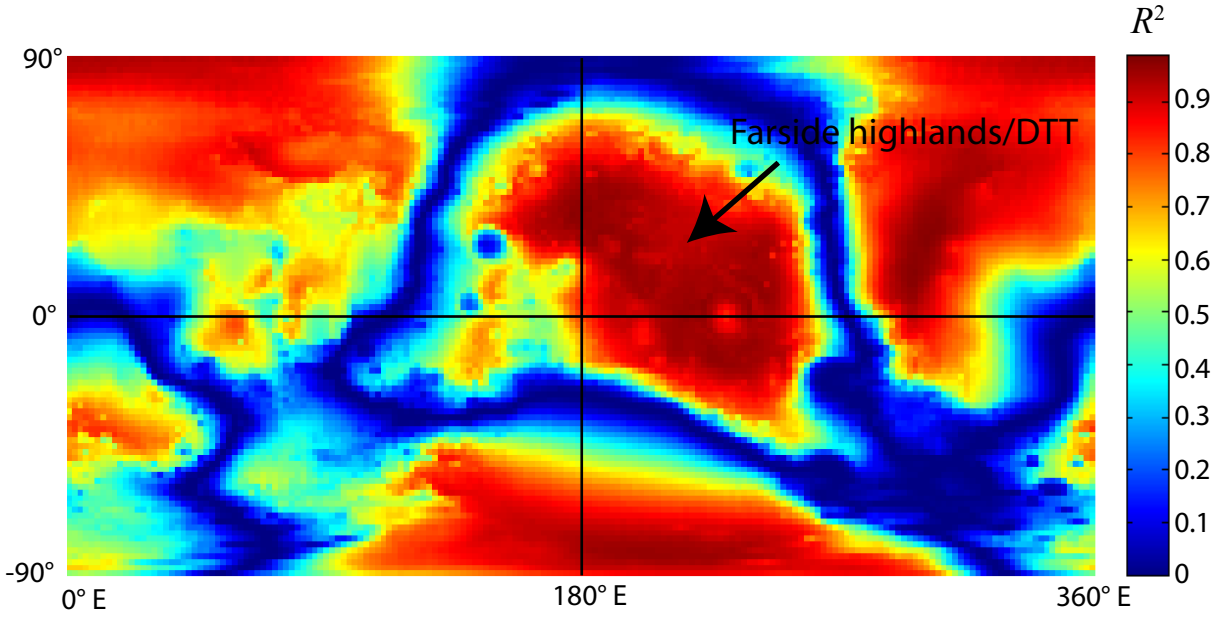
R^2
90°
0°
-90°
0° E
180° E
360° E
Farside highlands/DTT
0.9
0.8
0.7
0.6
0.5
0.4
0.3
0.2
0.1
0

Figure S6

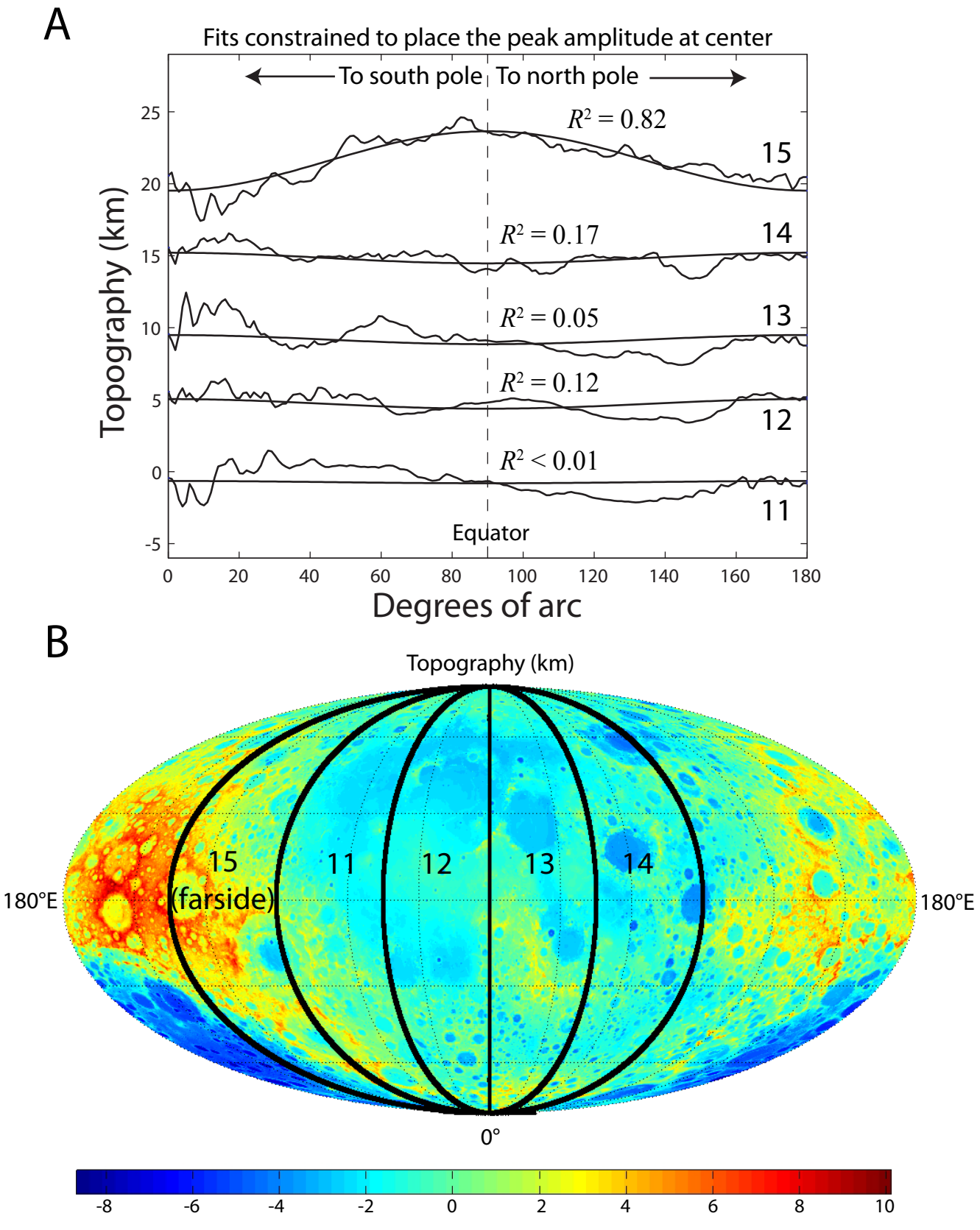
A
Fits constrained to place the peak amplitude at center
To south pole
To north pole
$R^2 = 0.82$
15
$R^2 = 0.17$
14
$R^2 = 0.05$
13
$R^2 = 0.12$
12
$R^2 < 0.01$
11
Equator
Topography (km)
Degrees of arc
B
Topography (km)
15
(farside)
11
12
13
14
180°E
180°E
0°

Figure S7

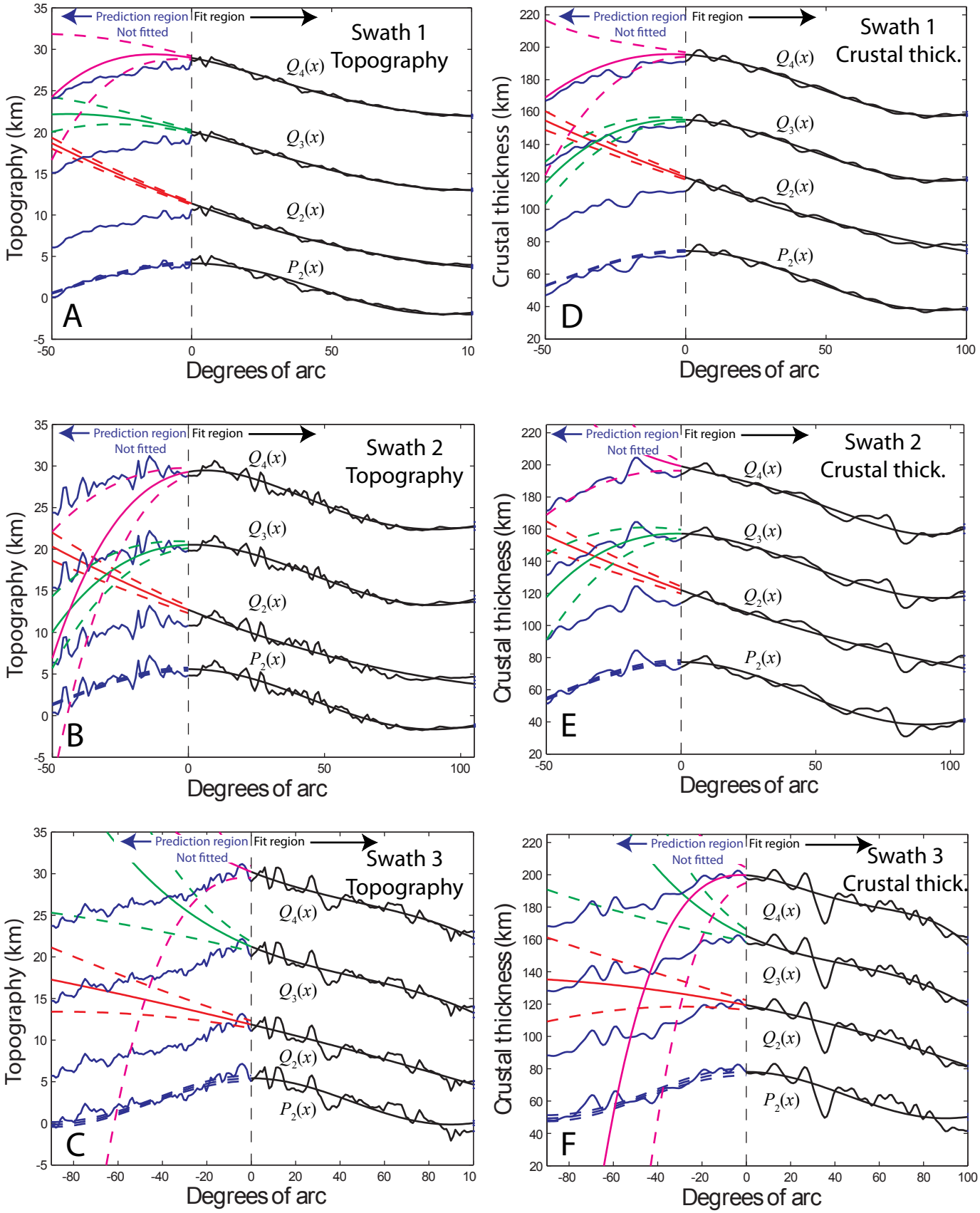
Prediction region
Not fitted
Fit region
Swath 1
Topography
$Q_4(x)$
$Q_3(x)$
$Q_2(x)$
$P_2(x)$
A
Topography (km)
Degrees of arc
Swath 1
Crustal thick.
D
Crustal thickness (km)
Swath 2
Topography
B
Swath 2
Crustal thick.
E
Swath 3
Topography
C
Swath 3
Crustal thick.
F

Figure S8

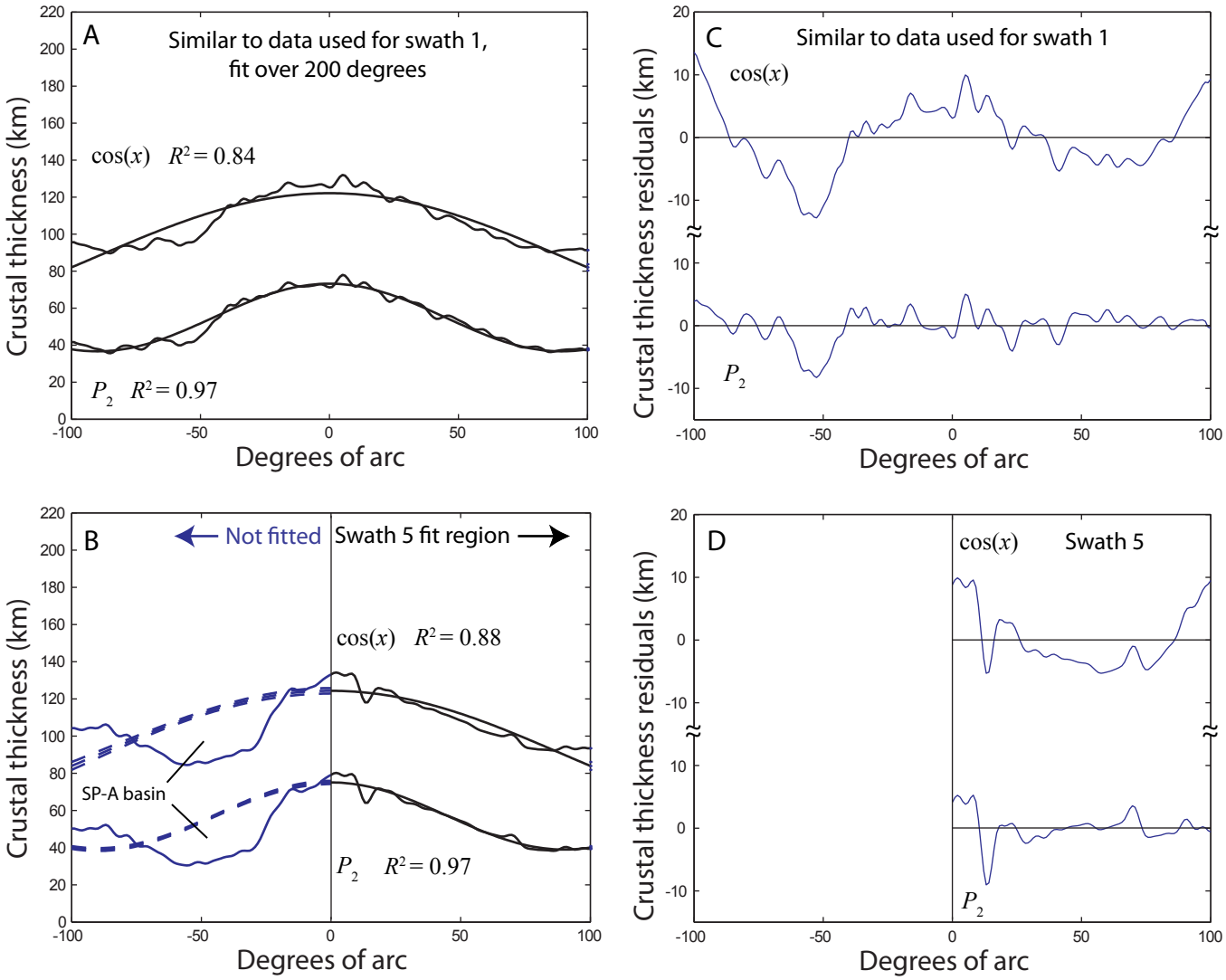
A
Similar to data used for swath 1,
fit over 200 degrees
cos(x) R² = 0.84
P2 R² = 0.97
Crustal thickness (km)
Degrees of arc
C
Similar to data used for swath 1
cos(x)
P2
Crustal thickness residuals (km)
Degrees of arc
B
Not fitted
Swath 5 fit region
cos(x) R² = 0.88
SP-A basin
P2 R² = 0.97
Crustal thickness (km)
Degrees of arc
D
cos(x)
Swath 5
P2
Crustal thickness residuals (km)
Degrees of arc

Figure S9

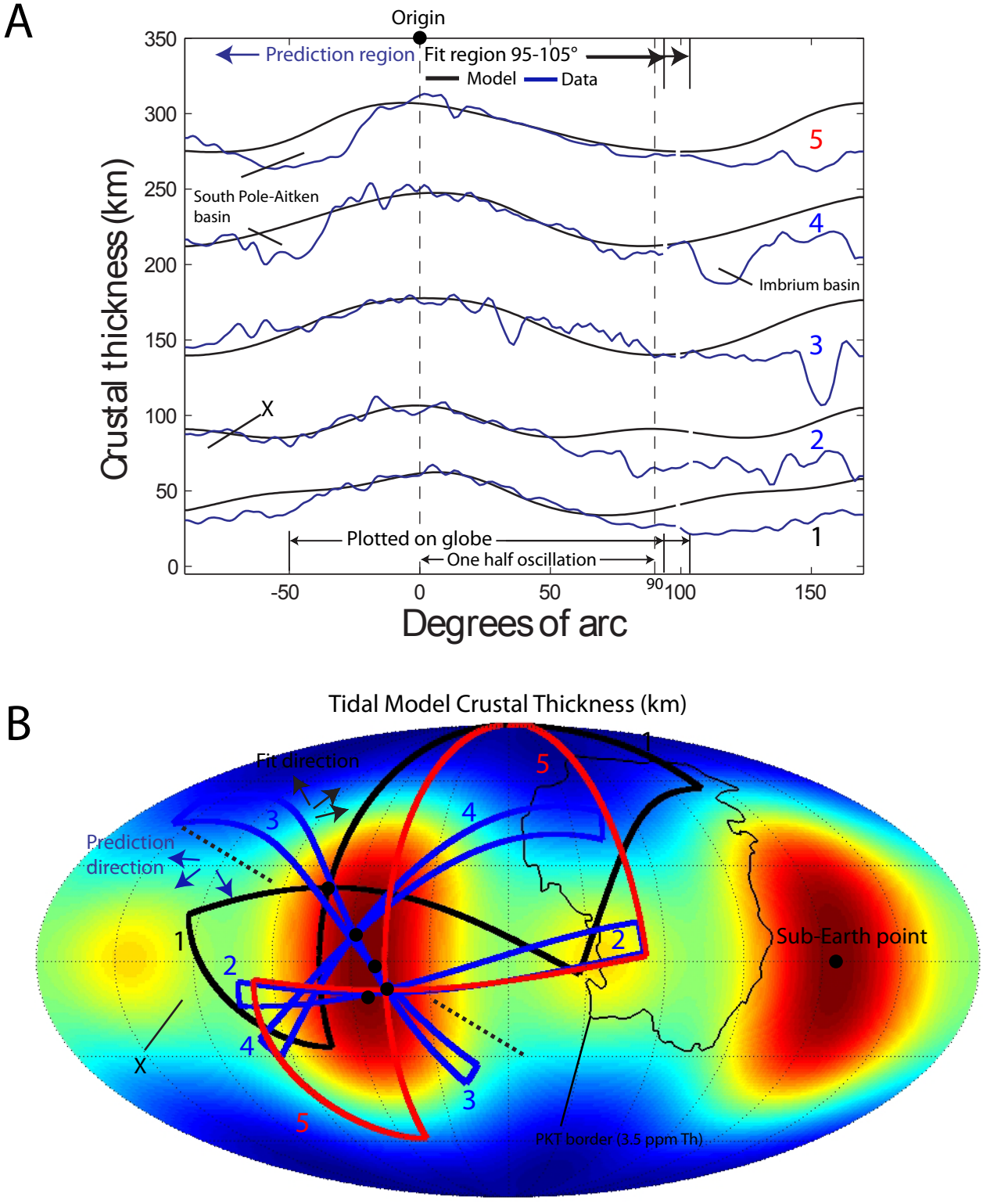
A
Origin
Prediction region
Fit region 95-105°
Model
Data
Crustal thickness (km)
South Pole-Aitken basin
Imbrium basin
X
Plotted on globe
One half oscillation
Degrees of arc
B
Tidal Model Crustal Thickness (km)
Fit direction
Prediction direction
Sub-Earth point
PKT border (3.5 ppm Th)
Tidal reference frame shifted 35° east. Compare with Fig. 1 and Fig. S3.

Figure S10

A

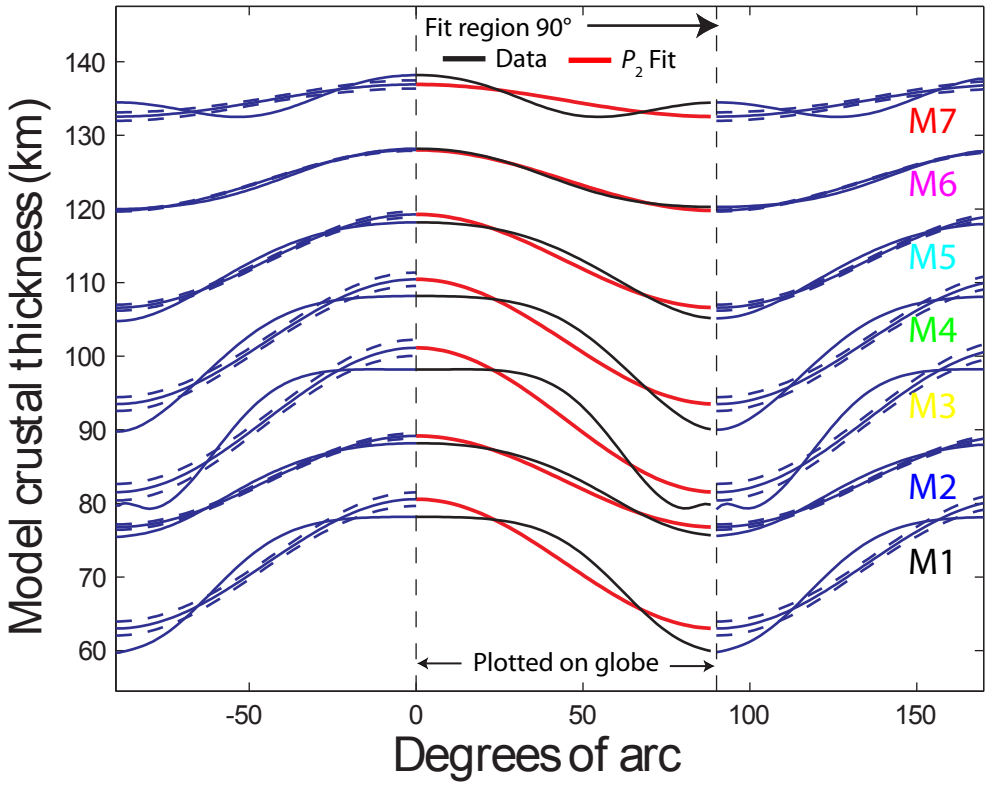

B

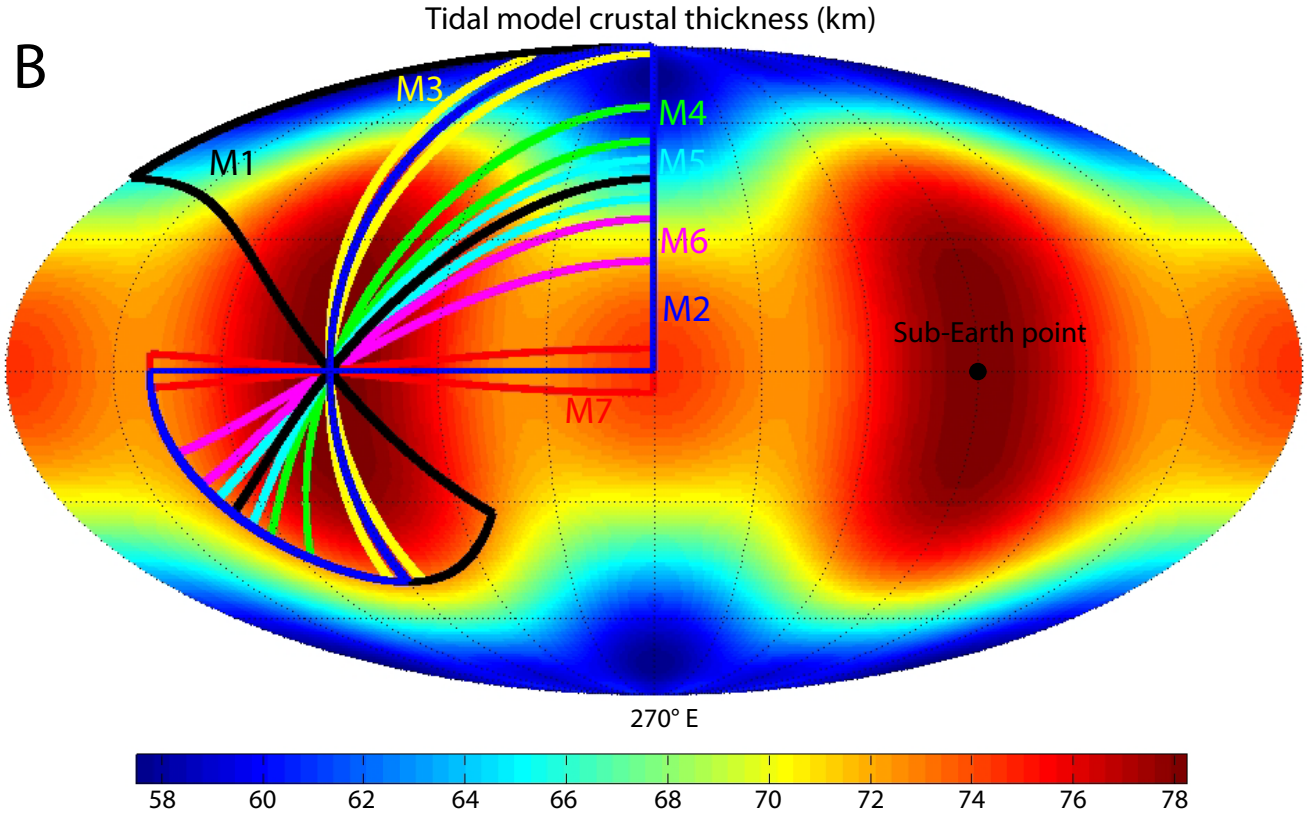

Figure S11

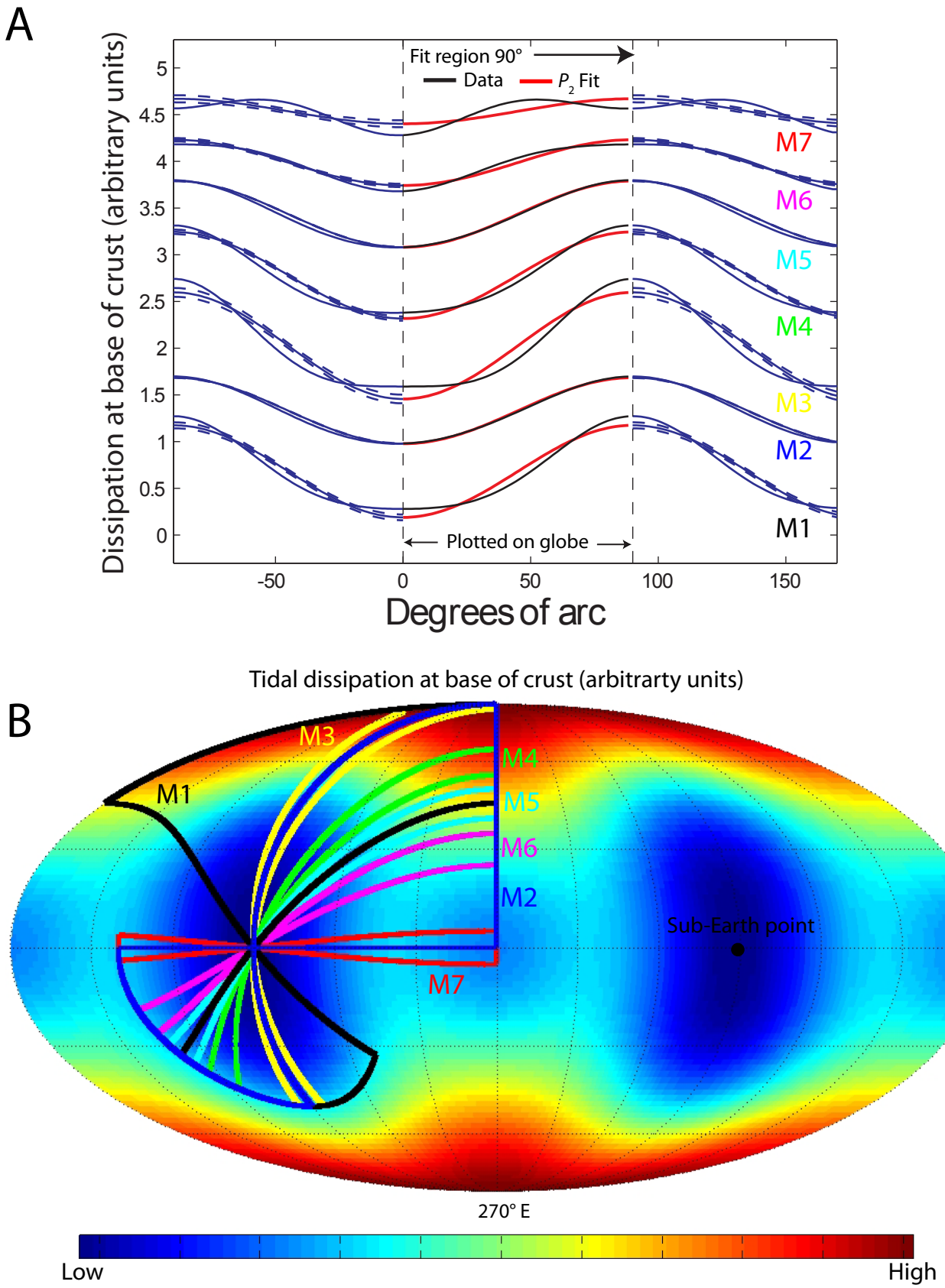
A
Fit region 90°
Data
P_2 Fit
M7
M6
M5
M4
M3
M2
M1
Plotted on globe
Dissipation at base of crust (arbitrary units)
Degrees of arc
B
Tidal dissipation at base of crust (arbitrarty units)
M3
M1
M4
M5
M6
M2
M7
Sub-Earth point
270° E
Low
High

Figure S12

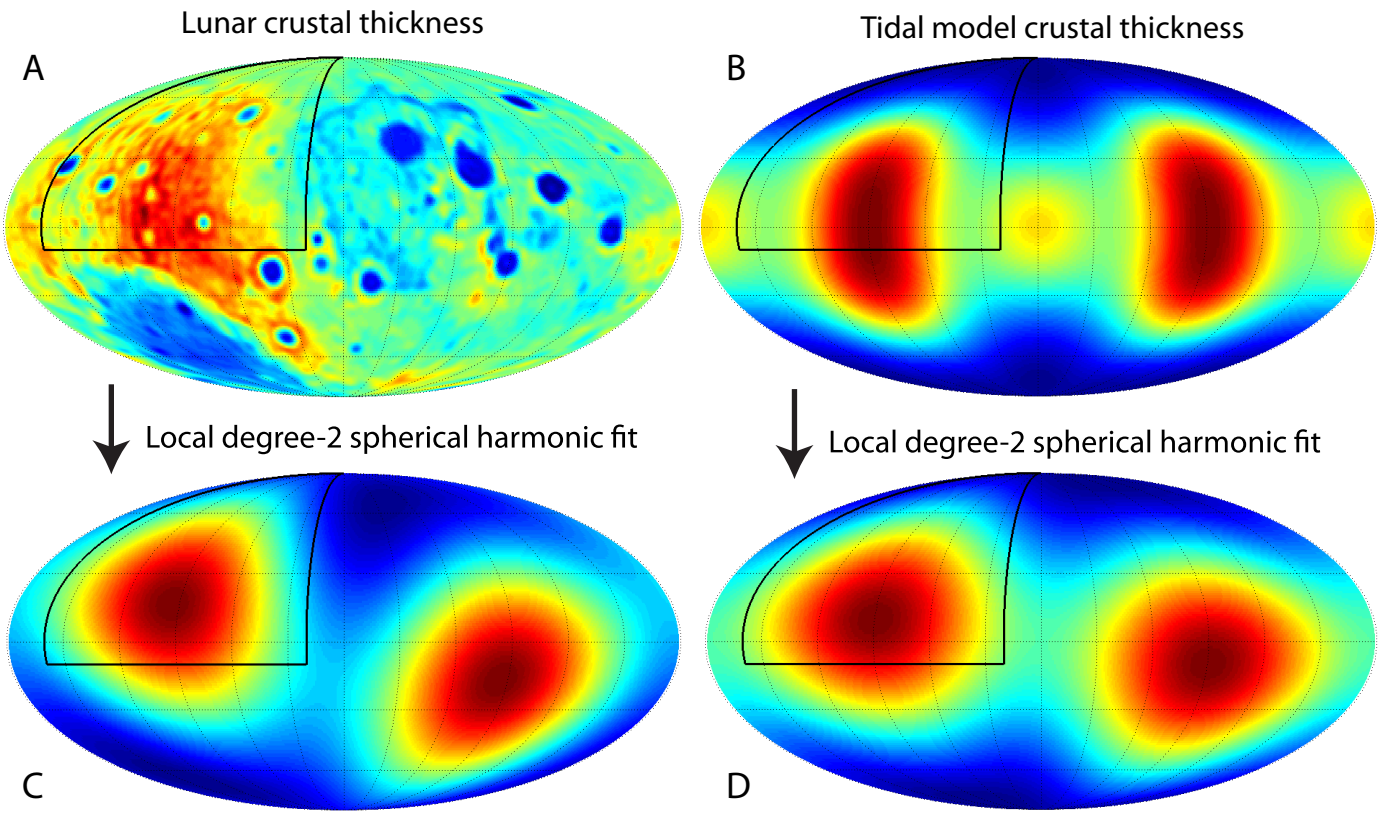
Lunar crustal thickness
A
Tidal model crustal thickness
B
Local degree-2 spherical harmonic fit
Local degree-2 spherical harmonic fit
C
D

Figure S13

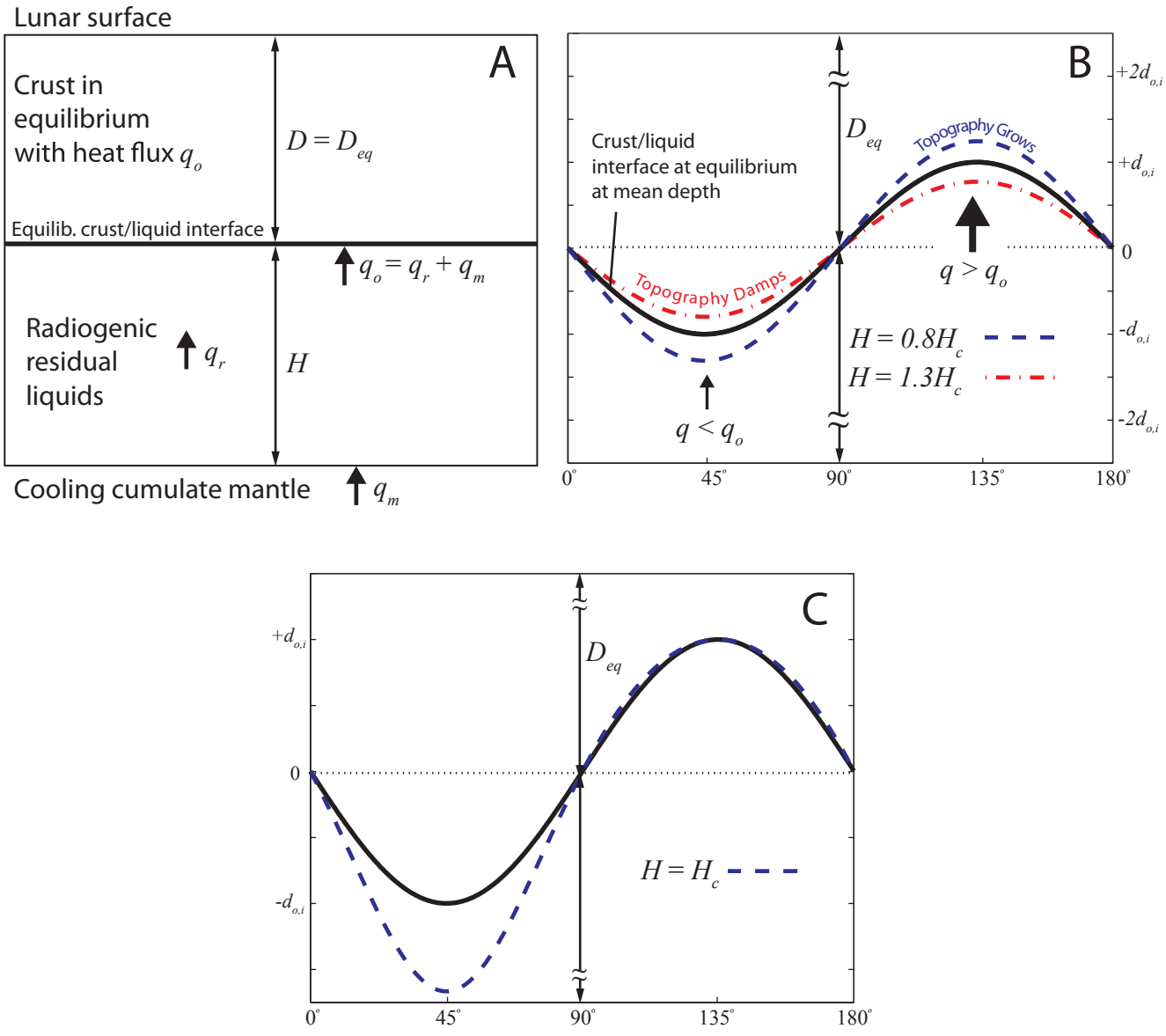
Lunar surface
A
Crust in equilibrium with heat flux q_o
$D = D_{eq}$
Equilib. crust/liquid interface
$q_o = q_r + q_m$
Radiogenic residual liquids
q_r
H
Cooling cumulate mantle
q_m
B
Crust/liquid interface at equilibrium at mean depth
D_{eq}
Topography Grows
Topography Damps
$q > q_o$
$q < q_o$
$H = 0.8H_c$
$H = 1.3H_c$
$+2d_{o,i}$
$+d_{o,i}$
0
$-d_{o,i}$
$-2d_{o,i}$
0°
45°
90°
135°
180°
C
$+d_{o,i}$
D_{eq}
0
$-d_{o,i}$
$H = H_c$
0°
45°
90°
135°
180°

Figure S14

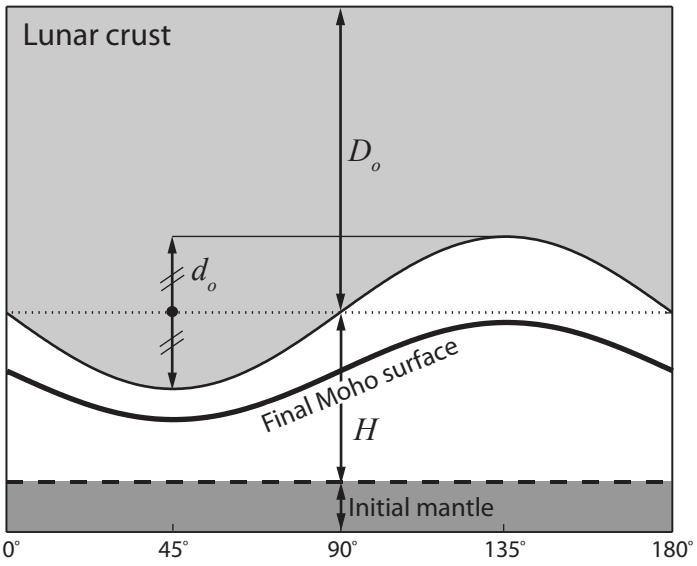
Lunar crust
D_o
d_o
Final Moho surface
H
Initial mantle
0°
45°
90°
135°
180°

Figure S15

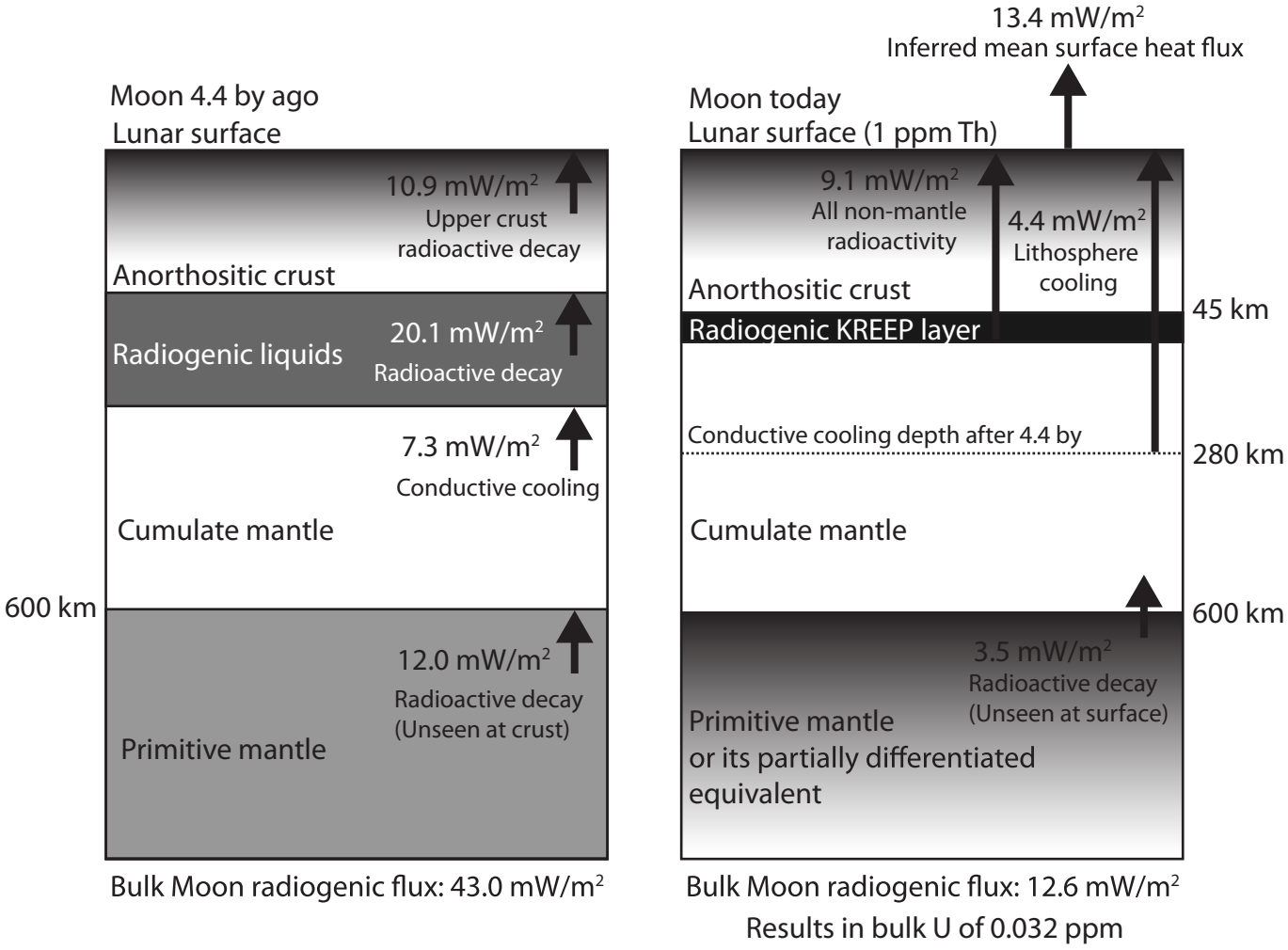
Moon 4.4 by ago
Lunar surface
10.9 mW/m²
Upper crust
radioactive decay
Anorthositic crust
Radiogenic liquids
20.1 mW/m²
Radioactive decay
7.3 mW/m²
Conductive cooling
Cumulate mantle
600 km
12.0 mW/m²
Radioactive decay
(Unseen at crust)
Primitive mantle
Bulk Moon radiogenic flux: 43.0 mW/m²
13.4 mW/m²
Inferred mean surface heat flux
Moon today
Lunar surface (1 ppm Th)
9.1 mW/m²
All non-mantle
radioactivity
4.4 mW/m²
Lithosphere
cooling
Anorthositic crust
45 km
Radiogenic KREEP layer
Conductive cooling depth after 4.4 by
280 km
Cumulate mantle
600 km
3.5 mW/m²
Radioactive decay
(Unseen at surface)
Primitive mantle
or its partially differentiated
equivalent
Bulk Moon radiogenic flux: 12.6 mW/m²
Results in bulk U of 0.032 ppm

Figure S16

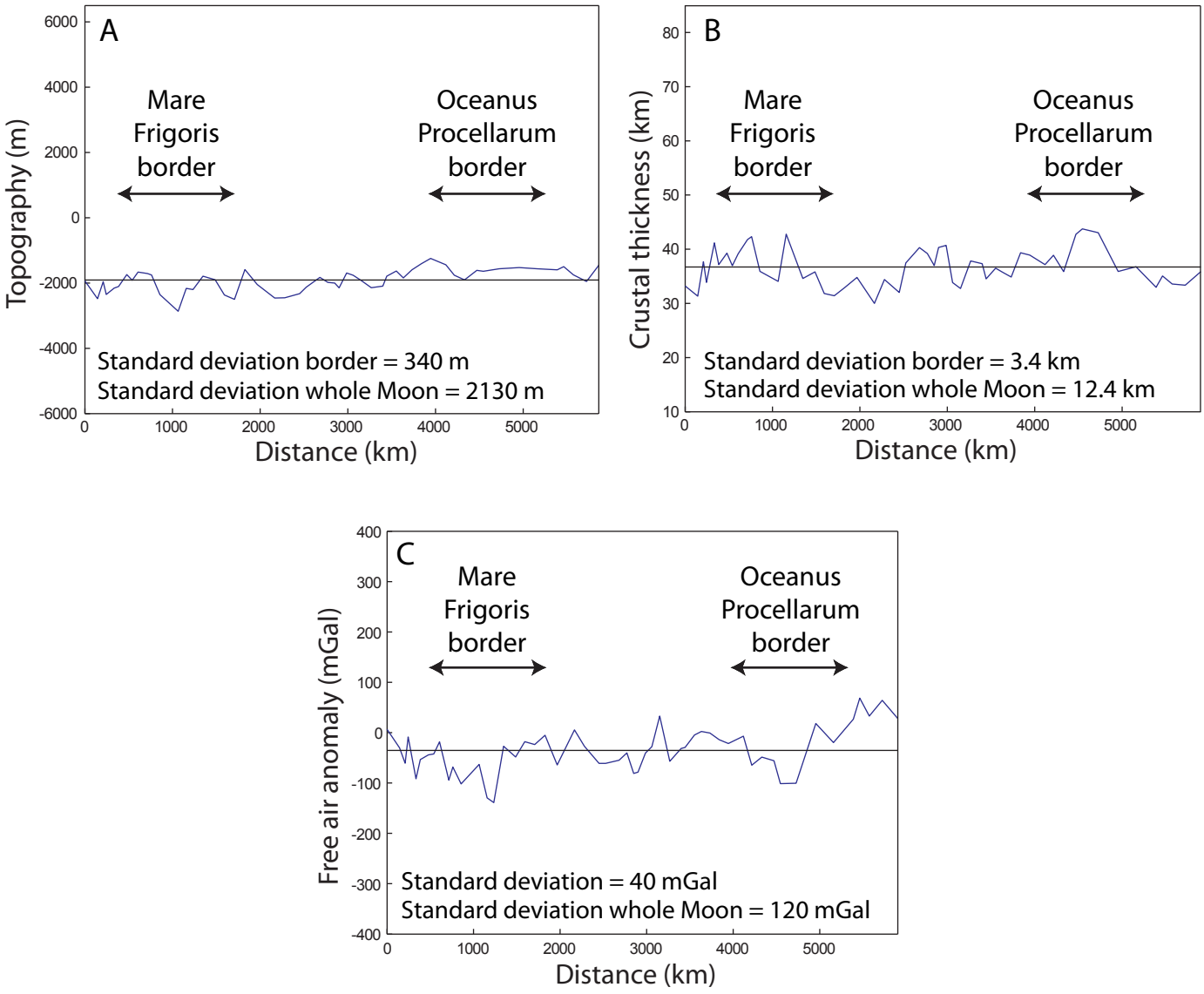
A
Mare Frigoris border
Oceanus Procellarum border
Topography (m)
Standard deviation border = 340 m
Standard deviation whole Moon = 2130 m
Distance (km)
B
Mare Frigoris border
Oceanus Procellarum border
Crustal thickness (km)
Standard deviation border = 3.4 km
Standard deviation whole Moon = 12.4 km
Distance (km)
C
Mare Frigoris border
Oceanus Procellarum border
Free air anomaly (mGal)
Standard deviation = 40 mGal
Standard deviation whole Moon = 120 mGal
Distance (km)

Figure S17